

# Modeling the RV jitter of early M dwarfs using tomographic imaging

É.M. Hébrard<sup>1,2,3\*</sup>, J.-F. Donati<sup>2,3</sup>, X. Delfosse<sup>4,5</sup>, J. Morin<sup>6</sup>, C. Moutou<sup>7,8</sup> and I. Boisse<sup>8</sup>

<sup>1</sup> Department of Physics and Astronomy, York University, Toronto, ON M3J 1P3, Canada

<sup>2</sup> CNRS-INSU; IRAP-UMR 5277, 14 Av. E. Belin, F-31400 Toulouse, France

<sup>3</sup> Université de Toulouse; UPS-OMP; IRAP; Toulouse, France

<sup>4</sup> Univ. Grenoble Alpes, IPAG, F-38000 Grenoble, France

<sup>5</sup> CNRS, IPAG, F-38000 Grenoble, France

<sup>6</sup> LUPM, Université Montpellier II, CNRS, UMR 5299, Place E. Bataillon, 34095 Montpellier, France

<sup>7</sup> CNRS, Canada-France-Hawaii Telescope Corporation, 65-1238 Mamalahoa Hwy, Kamuela, HI 96743, USA

<sup>8</sup> Aix-Marseille Université, CNRS, LAM, UMR 7326, 13388 Marseille, France

Accepted XXX. Received YYY; in original form ZZZ

## ABSTRACT

In this paper we show how tomographic imaging (Zeeman Doppler Imaging, ZDI) can be used to characterize stellar activity and magnetic field topologies, ultimately allowing to filter out the radial velocity (RV) activity jitter of M-dwarf moderate rotators. This work is based on spectropolarimetric observations of a sample of five weakly-active early M-dwarfs (GJ 205, GJ 358, GJ 410, GJ 479, GJ 846) with HARPS-Pol and NARVAL. These stars have  $v \sin i$  and RV jitters in the range 1–2 km s<sup>−1</sup> and 2.7–10.0 m s<sup>−1</sup> rms respectively.

Using a modified version of ZDI applied to sets of phase-resolved Least-Squares-Deconvolved (LSD) profiles of unpolarized spectral lines, we are able to characterize the distribution of active regions at the stellar surfaces. We find that dark spots cover less than 2% of the total surface of the stars of our sample. Our technique is efficient at modeling the rotationally modulated component of the activity jitter, and succeeds at decreasing the amplitude of this component by typical factors of 2–3 and up to 6 in optimal cases. From the rotationally modulated time-series of circularly polarized spectra and with ZDI, we also reconstruct the large-scale magnetic field topology. These fields suggest that bi-stability of dynamo processes observed in active M dwarfs may also be at work for moderately active M dwarfs. Comparing spot distributions with field topologies suggest that dark spots causing activity jitter concentrate at the magnetic pole and/or equator, to be confirmed with future data on a larger sample.

**Key words:** stars: magnetic fields - starspots – techniques : radial velocity - polarimetric – line : profile

## 1 INTRODUCTION

Lots of exoplanets were either detected or confirmed thanks to the radial velocity (RV) technique which allows one to detect exoplanets of various masses and sizes, from hot-Jupiters to super Earths. This is made possible thanks to the sensitivity and stability of current velocimeters. However, as an indirect method based on measuring spectral shifts, velocimetry is also sensitive to phenomena of intrinsic stellar origin capable of affecting spectra, and in particular to stellar activity. Whatever the precision of forthcoming instruments, we will remain confronted with this limitation, rendering Earth-like planets hard to detect, their spectral signatures being

much smaller than the activity-induced RV jitter, even for weakly active Sun-like stars.

Signals of stellar origin can occur on different timescales; some have a short period, typically ranging from minutes to hours (*e.g.*, flares, granulation), whereas some feature a longer period, ranging from days to year (*e.g.*, activity cycle, spot or convection inhibition from a strong magnetic field modulated by the rotation). Whatever the temporal timescale, most stellar phenomena causing spectral variability are related to magnetic fields and to the associated activity demonstrations. The modeling of the RV jitter is essential to all extrasolar planets searches, especially when orbital periods are larger than a few days and when the host stars exhibit activity phenomena occurring on timescales commensurate with the planetary signals of interest. The only way to improve the sensitiv-

\* E-mail: ehebrard@yorku.ca

ity of RV surveys to small planets is to characterize and model the activity jitter as well as possible.

To diagnose the RV jitter, several complementary approaches are commonly used, mostly making use of chromospheric activity indicators like excess flux in the cores of the H $\alpha$  and Ca II H&K, or measurements of spectral line asymmetries (with the bisector of the cross-correlation function). The idea is to check for periodic modulation of these proxies, in order to assess whether the observed RV signal is caused by activity rather than by a planet (see [Queloz et al. 2001](#)). The correlation between RVs and the slope of the bisector can in principle be used to correct for the effect of activity at a level of a few  $\text{m s}^{-1}$  ([Boisse et al. 2009](#)). The accuracy to which the RV jitter can be corrected with this method largely depends on various parameters, e.g., the distribution of spots, the stellar inclination, the rotational broadening of line profiles. An alternative method is based on exploiting complementary information from velocimetric and high-cadence photometric simultaneous/contemporaneous observations, and make use of the predicted relationship between the photometric and RV signatures of spots ([Aigrain et al. 2012](#); [Haywood et al. 2014](#)). These studies found that RV modulation caused by spots can be reliably modeled using the photometric flux  $F$  and its first derivative  $F'$ . Other studies ([Meunier et al. 2010](#); [Borngniet et al. 2015](#)) use the Sun as a star to predict the effect of activity on conventional activity diagnostics, taking advantage of the wealth of existing data. However activity, and its correlation to RV jitter, depends strongly on spectral type, stellar mass and rotation rate, and so far, no studies are available to reliably extrapolate the solar case to all types of active stars.

Besides, the large majority of extrasolar planets up to now was found around main-sequence stars of spectral types ranging from late-F to early-M. Despite M dwarfs are the most abundant type of stars, their intrinsic faintness in the visible domain caused them to be underrepresented in RV surveys with existing instruments. RV and transiting survey demonstrate that planets is very frequent around M-dwarfs, in particular Earth and Super-Earth at short period, ([Bonfils et al. 2013](#); [Dressing & Charbonneau 2015](#)). Moreover, due to their low masses, these targets are interesting for Earth-like planet hunting; an orbiting planet of a given mass and orbital distance generates a higher reflex motion when orbiting around a M dwarf than around a solar type star. Therefore, observations of low-mass stars is a promising option to increase our sensitivity to Earth-like planets. Due to the low photospheric temperature of M-dwarfs, the planetary orbits that are located in the habitable zone (HZ) of the host star (*i.e.*, within the proper range of orbital distances where liquid water may be stable at the planet surfaces) move closer in. For instance, for a M-dwarf with a typical mass of  $0.5 M_{\odot}$  (like those studied in our paper), the HZ lies in a range  $0.2 - 0.45$  AU (see [Kasting et al. 2014](#)). It corresponds to orbital periods in the range  $36 - 157$  d, *i.e.*, to RV semi-amplitude of  $1.5 - 0.96 \text{ m s}^{-1}$  for a planet mass of  $5 M_{\oplus}$  (as opposed to  $0.4 \text{ m s}^{-1}$  for a planet of the same mass orbiting in the HZ of a Sun-like star).

Despite the gain in the RV sensitivity to small planets that M dwarfs allow to achieve, modeling and filtering efficiently the activity jitter of the host stars remain essential, given that this activity jitter is still at best comparable in size to the RV signal we aim at detecting, and with a similar period as orbital periods of planets within the HZ (see, *e.g.*, [Forveille et al. 2009](#); [Robertson et al. 2014](#)). So far, studies of late M dwarfs have shown that these stars exhibit significant RV jitter mostly induced by dark spots at their surfaces, implying that efficient observational strategies are mandatory to reliably disclose planets orbiting around them (*e.g.*, [Barnes et al. 2014](#), for M5-M9). These studies rely on simulations and/or

spectroscopic and/or photometric survey to diagnose the activity jitter. However, mainly due to their low luminosity in the optical to nIR domain, whether the predominant spot pattern is random, uniform or concentrated at active latitudes remains unclear ([Barnes et al. 2011](#); [Andersen & Korhonen 2015](#), and references therein). In this paper, we propose to explore a new method based on simultaneously studying the RV jitter caused by activity, and Zeeman signatures reflecting the large-scale magnetic field at the origin of activity to (i) investigate the level to which spot distributions causing the RV jitter relates to magnetic topologies and (ii) devise a new technique based on spectropolarimetric data to filter out activity on a sample of early M dwarfs.

We present the results of a spectropolarimetric campaign carried out on September 2013 - September 2014. After a brief description of the stellar sample in Sec. 2.1 and of the data reduction procedure in Sec. 2.2, we present the results obtained by analyzing circularly polarized spectra (Stokes  $V$ ) in Sec. 3. The stellar activity diagnostic is introduced in Sec. 4, and is followed by the analysis of the rotational modulation of the RV jitter, and of its modeling in Sec. 5. The magnetic field and brightness reconstruction procedure using Zeeman-Doppler imaging (ZDI) are presented in Sec. 3.3 and 5.1. We summarize the main outcome of this analysis and discuss its implications in Sec. 6.

## 2 SPECTROPOLARIMETRIC OBSERVATIONS

### 2.1 Stellar sample

Our stellar sample includes five weakly-active, early-M dwarfs with different rotation periods (spanning 11-33 d) and stellar masses ( $0.35$ - $0.61 M_{\odot}$ ). The selected targets are among the most observed and best characterized ones in the ESO/HARPS RV survey of M dwarfs ([Bonfils et al. 2013](#)), guaranteeing that their activity jitters are known (with rms in the range  $2.7$ - $10.0 \text{ m s}^{-1}$ ) and detectable. So far no planets are detected for the stars of the sample. The five targets are known to show RV variations mostly caused by activity ([Bonfils et al. 2013](#); [Donati et al. 2008](#)). The main properties of this stellar sample, both inferred from this work or extracted from previous publications, are listed in Table 1. The sample is complementary to those studied in spectropolarimetry by [Donati et al. \(2008\)](#); [Morin et al. \(2008b, 2010\)](#)

Stellar masses are derived from the empirical mass-luminosity relationship of [Delfosse et al. \(2000\)](#) together with parallaxes and K-band photometry (both taken from *Hipparcos* catalogue, [Koen et al. 2010](#)). The luminosity is deduced from the infrared K band photometry and J-K colors are converted into luminosities with the bolometric correction of [Leggett et al. \(2001\)](#). The stellar radius  $R_{\star}$  is estimated from the mass-radius relation given in [Baraffe et al. \(2015\)](#).

The line-of-sight-projected equatorial rotation velocity value ( $v \sin i$ ) is either taken from the literature ([Bonfils et al. 2012](#); [Forveille et al. 2009](#); [Donati et al. 2008](#); [Bonfils et al. 2007](#)), or constrained thanks to the ZDI code (see Sec. 3.3). For the whole sample, the  $v \sin i$  is lower than  $2 \text{ km s}^{-1}$  (see Table 1) and the precision on  $v \sin i$  estimate does not exceed  $0.5 \text{ km s}^{-1}$ . The  $v \sin i$  values are compatible with the amount of rotational broadening observed in the spectra of our sample of stars. The measurement of the stellar rotation period  $P_{\text{rot}}$  is presented in detail in Sec. 3.2. We found rotation periods ranging from 13.83 to 33.63 d. Finally, the inclination of the rotation axis with respect to the line of sight,  $i$ , is estimated from the tomographic technique, with a precision of typically  $\pm 10^{\circ}$  ([Morin et al. 2010](#), for more details).

Nom	ST	J	K	distance pc	$M_{\star}$ $M_{\odot}$	$L_{\star}$ $L_{\odot}$	$R_{\star}$ $R_{\odot}$	$v \sin i$ $\text{km s}^{-1}$	$i$ $^{\circ}$	$P_{\text{rot}}$ d	$\text{rms}_0$ $\text{m s}^{-1}$	$\sigma_0$ $\text{m s}^{-1}$
GJ 205	M1	5.0	3.90	5.66±0.04	0.63±0.06	0.061±0.006	0.55±0.08	1	60	33.63 ± 0.37 <sup>a</sup>	2.71	1.45
GJ 358	M2	6.90	6.06	9.47±0.15	0.42±0.04	0.023±0.002	0.41±0.06	1	60	25.37 ± 0.32 <sup>a</sup>	5.10	2.08
GJ 410	M0	6.52	5.68	11.77±0.15	0.58±0.06	0.055±0.005	0.53±0.08	2	60	13.83 ± 0.10 <sup>c</sup>	10.0	3.28
GJ 479	M2	6.86	6.02	9.69±0.22	0.43±0.04	0.025±0.003	0.42±0.06	1	60	24.04 ± 0.75 <sup>b</sup>	5.45	2.02
GJ 846	M0	6.20	5.56	10.24±0.16	0.60±0.06	0.059±0.006	0.54±0.08	2	60	10.73 ± 0.10 <sup>b</sup>	3.30	2.45

**Table 1.** Stellar parameters of the M dwarfs sample. Columns 1-8 list the star name, its spectral type (ST), its J & K band magnitude and its distance (coming from the Hipparcos catalogue [Koen et al. 2010](#)), the stellar mass, luminosity and theoretical radius ([Baraffe et al. 2015](#)). The columns 9-12 respectively list the measured  $v \sin i$  (with a estimated error of  $\pm 0.5 \text{ km s}^{-1}$ ), the assessment of the stellar inclination angle  $i$  (with a estimated error of  $\pm 10^{\circ}$ ), the rotation period of the star  $P_{\text{rot}}$ , the rms of RV measurements and the average noise  $\sigma_0$  on the RV measurements. These four last parameters come from this study.

<sup>a</sup> compatible with [Kiraga & Stepien \(2007\)](#), <sup>b</sup> compatible with [Bonfils et al. \(2012\)](#), <sup>c</sup> compatible with [Donati et al. \(2008\)](#).

Instrument	Tel. (m)	Spectral domain (nm)	$R$	$\eta$ (%)
NARVAL	2	350 - 1050	68 000	10-15
HARPS-Pol	3.6	368 - 691	100 000	2-3

**Table 2.** Main characteristics of NARVAL ([Donati 2003](#)) and HARPS-Pol ([Snik et al. 2011](#)): Column 1 gives the instrument name, column 2 the diameter of the telescope primary mirror, column 3 the spectral domain (covered in a single exposure), column 4 the resolving power  $R$  and column 5 the estimated peak instrument throughput  $\eta$  (at  $\sim 550\text{nm}$ ).

Name	BJD <sub>0</sub> (+ 2456000)	$n_{\text{obs}}$	S/N	Cycle
GJ 205	569.88	22	170 - 228	0.000 - 3.523
GJ 358	675.70	23	70 - 133	0.000 - 2.880
GJ 410	673.88	29	79 - 125	1.000 - 6.199
GJ 479	778.00	23	63 - 146	0.024 - 2.684
GJ 846 (#2)	829.87	11	189 - 318	25.764 - 31.848
GJ 205	569.88	4	308 - 454	1.623 - 2.186
GJ 410	673.88	13	169 - 303	0.558 - 7.542
GJ 846 (#1)	546.46	15	91 - 158	0.000 - 8.709

**Table 3.** Synthetic journal of HARPS-Pol (top panel) and NARVAL (bottom panel) observations. The first days of observation is given in columns 2. Column 3 indicates the number of collected spectra. Columns 4 lists the peak S/N (resp., per 0.85 and 2.6  $\text{km s}^{-1}$  velocity bin for HARPS-Pol (at 650 nm) and NARVAL (at 750 nm)) - we precise the minimum and maximum obtained values. Column 5 indicates the rotational cycle bounds (computed with the rotation period mentioned in Table 1 according to ephemeris given by Eq 1).

## 2.2 Instrumental set-up and data reduction

Observations presented here were collected during two observing campaigns with the HARPS<sup>1</sup> velocimeter ([Mayor et al. 2003](#); [Snik et al. 2011](#)) used in spectropolarimetric mode and in a smaller extent with the NARVAL<sup>2</sup> spectropolarimeter ([Donati 2003](#); [Donati & Landstreet 2009](#)).

We observed from October 2013 to September 2014 with HARPS-Pol. In this instrument two optical fibers convey the stellar light, split into two orthogonal polarization states, from the Cassegrain focus of the telescope to the spectrograph. The instrument covers the 368-691 nm wavelength domain in a single exposure, at a resolving power of 100 000. An additional campaign was carried out from September 2013 to April 2014 with NARVAL, providing full coverage of the optical domain from 350 to 1050 nm in a single exposure, at a resolving power of 65 000, and into two orthogonal polarization states. The main characteristic of the instruments are listed in Table 2.

A spectropolarimetric observation consists of four sub-exposures taken at different azimuths of the quarter-wave plate (for HARPS-Pol) / half-wave rhombs (for NARVAL) relative to the optical axis of the beam splitter. The corresponding frames are combined together to produce a set of Stokes  $I$  (unpolarized intensity) and Stokes  $V$  (circularly polarized) spectra. Although it is possible to extract polarization spectra from two sub-exposures only, using four allows us to eliminate all systematic errors or spurious polarization signatures at first order ([Donati et al. 1997](#)).

The peak signal-to-noise ratios (S/N) per CCD pixel range from 70 to 200 at 600 nm for HARPS-Pol spectra (for which the

CCD pixel size is 0.85  $\text{km s}^{-1}$ ), and from 230 to 480 at 700 nm for NARVAL spectra (for which the CCD pixel size is 2.6  $\text{km s}^{-1}$ ). It mostly depends on the star magnitude and weather/seeing conditions. An overview of the observations is presented in Table 3, and the detail journal of observations of each star is given in Appendix B.

Rotational cycles of each target are computed from Barycentric Julian Dates (BJDs) according to the ephemeris:

$$\text{BJD (d)} = \text{BJD}_0 + P_{\text{rot}} \cdot E, \quad (1)$$

in which  $E$  is the rotational cycle,  $\text{BJD}_0$  is the initial date chosen arbitrarily and  $P_{\text{rot}}$  is the stellar rotation period derived from the magnetic analysis (see Sec. 3.2).

The data extraction is carried out with LIBRE-ESPRIT, a fully automated dedicated pipeline that performs optical extraction of the spectra. The initial procedure is described in [Donati et al. \(1997\)](#), and was adapted to HARPS-Pol data to make it compliant with precision velocimetry.

We apply Least-Squares Deconvolution (LSD, [Donati et al. 1997](#)) to all the observations in order to gather all the available polarimetric information into a single synthetic profile. LSD is similar to cross-correlation in the sense that it extracts information from a large number of spectral lines through a deconvolution procedure (see [Donati et al. 1997](#) for more details). To extract Stokes  $V$  LSD profiles from circular polarization spectra, we use a mask of

<sup>1</sup> High Accuracy Radial velocity Planet Searcher and spectropolarimeter at the ESO/3.6m telescope in La Silla (Chile)

<sup>2</sup> the ESPaDOs twin at the 2m Telescope Bernard Lyot (TBL) atop Pic-du-Midi (France)

	$\rho$ in spectrum	$\rho$ in LSD profile
GJ 205	3.57	5.76
GJ 410	6.32	10.61
GJ846	5.04	8.70

**Table 4.** Resulting peak flux ratio  $\rho$  between NARVAL and Harps-Pol. Column 1 indicates the star name. Column 2 gives  $\rho$  computed from spectra, after having taken into account the pixel size differences and the telescope photon collecting power. Column 3 lists  $\rho$  obtained from LSD profiles and then this value also takes into account the size of the spectral domain.

atomic lines computed with an ATLAS local thermodynamic equilibrium (LTE) model of the stellar atmosphere matching the properties of our whole sample (Kurucz 1993). The final mask contains about 4000 moderate to strong atomic lines, with a known Landé factor, from 350 nm to 1082 nm. The use of atomic lines only for the LSD masks relies on former studies of early and mid M dwarfs (Donati et al. 2008; Morin et al. 2008b). Zeeman signatures are clearly detected in Stokes V LSD profiles for all stars of our sample with a maximum peak-to-peak amplitude varying from 0.1% to 0.5% of the unpolarized continuum level. We observe temporal variations of the intensity and of the shape of the Stokes V LSD profile due to rotational modulation for the whole stars of the sample (see Sec 3).

For the unpolarized spectra, we use a denser line mask to increase our sensitivity to profile distortions and to RV variations of these five slow rotators. The mask is derived from M-dwarf spectra previously collected with HARPS (Bonfils et al. 2013), and contains 9000 lines from 440 to 686 nm. With this procedure, Stokes I LSD profiles distortions are detected with a maximum amplitude varying from 0.001% to 0.01% of the unpolarized continuum level (see Sec. 5).

For the stars observed with both HARPS-Pol and NARVAL (i.e., GJ 205, GJ 410 and GJ 846), we can use the collected spectra to compare the instrument efficiency. NARVAL being on a 2m telescope and HARPS-Pol on a 3.6m telescope, the ratio of the collected flux is about 0.31 at the telescope. The NARVAL peak throughput at 550 nm is thus, *in fine*, about 5.0 times higher than that of HARPS-Pol, once the pixel size is taken into account (see Table 4, second column). LSD allows to add up information from the whole observed spectral domain. Including the gain associated to the larger spectral domain, NARVAL is in average 8.4 times more efficient than HARPS-Pol (see Table 4, third column). This explains why longitudinal field measurements secured with NARVAL are significantly more accurate than those derived from HARPS-Pol spectra despite the large ratio in telescope photon collecting power in favour of HARPS-Pol. For RV measurements, only HARPS-Pol spectra are used, NARVAL being limited to typical RV precisions of 20 m/s (Moutou et al. 2007).

### 3 MAGNETIC ANALYSIS

The goal of this section is to characterize the large-scale magnetic fields of the observed stars from the collected Stokes V LSD profiles. To get an overview of the magnetic data, we start by simply computing the longitudinal field  $B_l$ , i.e., the line-of-sight-projected magnetic vector averaged over the visible stellar hemisphere (Sec 3.1). From temporal variations of  $B_l$  and its rotational modulation, one can derive a reliable estimate of the stellar rotation period  $P_{\text{rot}}$  (Sec 3.2, and e.g., Morin et al. 2008b). In a second step, we apply ZDI to our time series of Stokes V LSD profiles, in order

to recover the topology of the large-scale field that generates the observed Zeeman signatures and their rotational modulation (see Sec 3.3).

#### 3.1 Longitudinal magnetic field

From each pair of Stokes I and V LSD profiles, we compute  $B_l$  (in Gauss) as follow (Donati et al. 1997):

$$B_l = \frac{-2.14 \times 10^{11}}{\lambda_0 g_{\text{eff}} c} \frac{\int vV(v)dv}{\int [I_c - I(v)]dv}, \quad (2)$$

with I and V denoting the unpolarized and circularly polarized LSD profiles,  $I_c$  the continuum level,  $v$  the radial velocity in  $\text{km s}^{-1}$ ,  $c$ , the speed of light in  $\text{km s}^{-1}$ ,  $\lambda_0$  the central wavelength in nm and  $g_{\text{eff}}$  the effective Landé factor.  $B_l$  is a simple magnetic field proxy one can easily extract, but which conveys little information on the likely complexity of the magnetic field geometry.

#### 3.2 Period determination

To estimate the stellar rotation period we first fit  $B_l$  with a multiple sine fit (fundamental period + the first harmonic). The explored period range spans  $0.5 \times$  to  $2 \times$  the value found in the literature. We choose  $P_{\text{rot}}$  that minimizes  $\chi_r^2$ , defined as the reduced  $\chi^2$  of the multiple sine fit to the  $B_l$  data. We compare this value to the period found computing the Lomb-Scargle periodogram of the  $B_l$  data (Lomb 1976; Scargle 1982; Zechmeister & Kürster 2009). This periodogram estimates the power associated to each period in the explored  $P_{\text{rot}}$  interval. To assess the chance that the strongest peak of the derived periodogram is caused by noise in the observations rather than by a true signal, we compute the 10% and 1% false alarm probabilities (FAPs) as defined in Zechmeister & Kürster (2009).

- GJ 358 : The resulting curves for GJ 358 are presented Fig. 1. We note that  $B_l$  remains mainly negative (averaged value of  $-32.0 \pm 1.5$  G), with a peak-to-peak amplitude of 70 G. The variations are periodic and well-fitted ( $\chi_r^2 = 1.0$ ) with a multiple sine fit at  $P_{\text{rot}} = 25.37 \pm 0.32$  d ( $1\sigma$  error bar). This period is in agreement with the period of  $\sim 25.26$  d given by Kiraga & Stepien (2007) from a photometric survey, as well as with the period found computing the Lomb-Scargle periodogram and associated with a FAP much lower than 1% (Fig. 1, bottom panel).

- GJ 479 : We observe a similar behaviour for  $B_l$  of GJ 479, with a rotation period of  $24.04 \pm 0.75$  d (see Fig. C1), in good agreement with the period estimated in a range 23-24 d by Bonfils et al. (2012). As indicated in the periodogram of  $B_l$  data, and contrary to the previous case, the first harmonic is essential to fit the data down to  $\chi_r^2 = 1.0$ .

- GJ 410 : For GJ 410 (Fig. 2),  $B_l$  varies periodically and exhibits regular sign switches; the averaged value is  $3.0 \pm 0.5$  G. The best period we derive from fitting  $B_l$  measurements is equal to  $13.83 \pm 0.10$  d, in agreement with the former study of Donati et al. (2008) ( $13.51 \pm 0.12$  d) and the Lomb-Scargle periodogram (see Fig. 2, FAP < 1%). This is one of the most active stars of our sample.

- GJ 205 : For GJ 205, we derive  $P_{\text{rot}} = 33.63 \pm 0.37$  d. To fit the data down to  $\chi_r^2 = 1.0$ , the fundamental period and

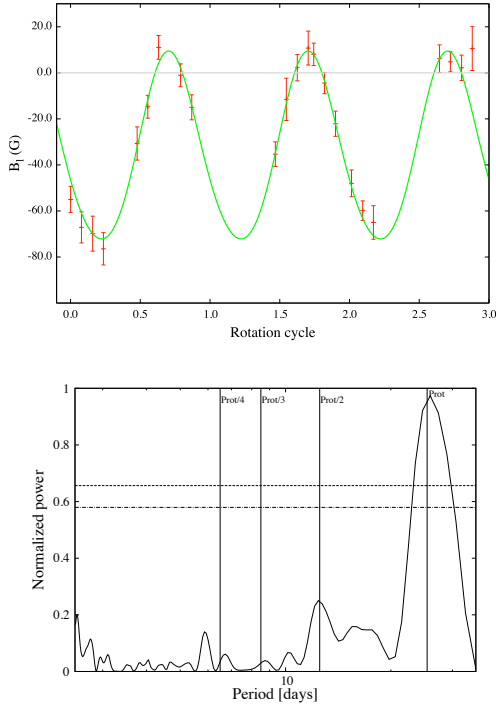


**Figure 1.** *Top:*  $B_l$  measurements of GJ 358 from HARPS-Pol spectra are shown as red dots (with  $\pm 1\sigma$  error bars). The green line depicts a multiple sine fit (fundamental + 1st harmonic) to the  $B_l$  measurements. The horizontal grey line represent the 0 G level. *Bottom:* Lomb-Scargle periodogram of  $B_l$  and the FAP at 1% (dashed line) and 10% (dotted-dashed line). The vertical lines depict  $P_{\text{rot}}$  and its three first harmonics  $P_{\text{rot}}/2$ ,  $P_{\text{rot}}/3$  and  $P_{\text{rot}}/4$ .

its first harmonic  $P_{\text{rot}}/2$  are needed. This is confirmed with the Lomb-Scargle periodogram whose strongest peak is at 16.8 d, i.e.,  $P_{\text{rot}}/2$  (FAP < 1%, see Fig. C2), and with the former photometric study of Kiraga & Stepien (2007) ( $\sim 33.61$  d).

- GJ 846 : For GJ 846, we only secured 11 measurements in July-September 2014 with HARPS-Pol and 15 measurements in September-December 2013 with NARVAL, spread over 6 and 9 rotation cycles respectively. The amplitude of the  $B_l$  variations changes between the two observation epochs: we first observe variations with a peak-to-peak amplitude of  $10 \pm 2$  G (averaged value  $1.4 \pm 0.5$  G), then variations with a peak-to-peak amplitude of  $20 \pm 4$  G (averaged value =  $6.0 \pm 1.5$  G).  $B_l$  keeps the same (positive) sign during the two runs. We derive a period equal to  $10.73 \pm 0.10$  d. This period is in good agreement with the periodicity of 10.7 d found in Bonfils et al. (2012).

Our observations thus demonstrate clearly that the spectropolarimetric data provides us with an accurate measurement of  $P_{\text{rot}}$ . In Sec. 4 we will demonstrate that spectropolarimetry is more efficient than usual proxies ( $H\alpha$  or the full width at half-maximum FWHM) to determine the rotational period, and that  $P_{\text{rot}}$  is a key parameter to track the origin of the activity signal (i.e., the magnetic field)

### 3.3 Magnetic imaging

To recover the parent large-scale magnetic field from time series of rotationally-modulated Zeeman signatures, we use the ZDI to-

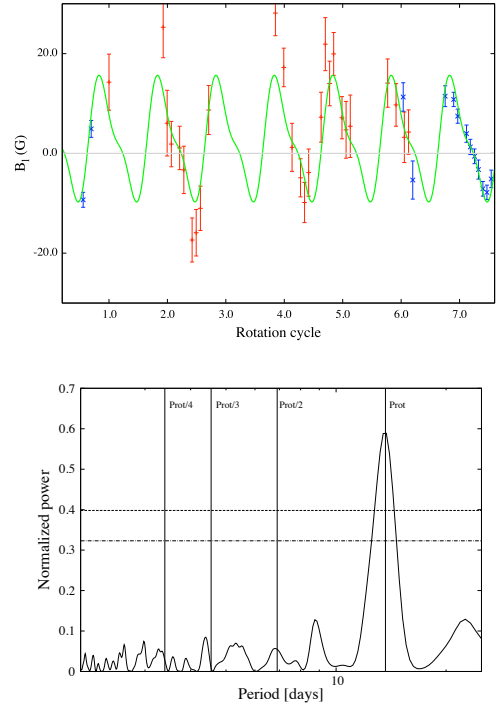


**Figure 2.** Same as Fig. 1 for GJ 410. Measurements from HARPS-Pol spectra are shown in red, while those from NARVAL spectra are shown in blue. Note the much smaller error bars on NARVAL  $B_l$  measurements, despite the 3.2 $\times$  smaller photon collecting power of TBL

mographic imaging technique. ZDI has been largely tested and improved since the initial release of Brown et al. (1991) (see, e.g., Donati et al. 2006b; Morin et al. 2008b). ZDI assumes that profile variations are mainly due to rotational modulation (plus some amount of differential rotation, if needed), and can turn series of circular polarization Stokes  $V$  LSD profiles into maps of the parent magnetic topology. The longitudinal and latitudinal resolution depends mainly on  $v \sin i$ ,  $i$ , and the phase coverage of the observations.

In our imaging procedure, we use spherical harmonics (SH) to describe the large-scale field, allowing in particular to reliably recover both simple and complex topologies (see, e.g., Donati 2001; Donati et al. 2006b).  $\mathbf{B}$  can be written as the sum of a poloidal and a toroidal component; their expressions can be found in Donati et al. (2006a). The parameters  $\alpha_{l,m}$ ,  $\beta_{l,m}$  and  $\gamma_{l,m}$ , noting the SH coefficients (with  $l$  denoting the degree of the mode, and  $m \in [0; l]$  its order), describe, respectively, the radial poloidal, non-radial poloidal and toroidal components of the magnetic field. The energy associated with the axisymmetric ( $m < l/2$ ) and non-axisymmetric modes of the poloidal field component, as well as that of the poloidal and toroidal components, can be estimated directly from the coefficients of the SH expansion. For the slow rotators considered here, most spatial information we can recover about the field concentrates in modes with orders equal to or lower than 5 (see, e.g., Morin et al. 2008b).

To compute synthetic circular polarization profiles, the surface of the star is divided into 5000 cells of similar projected areas (at maximum visibility), whose contribution to the integrated Stokes  $I$  and  $V$  LSD profiles depends on the RV of each cell, on the local field strength and orientation, on the location of the cell

and its projected area, on the rotation cycle, and on the local surface brightness of the photosphere (assumed to be uniform at this stage). To model the local unpolarized Stokes  $I$  and the local circular polarized Stokes  $V$  profiles (resp.  $I_{l,j}$  and  $V_{l,j}$ ) at each cell  $j$  in presence of magnetic fields, we use Unno-Rachkovsky's (UR) equations (e.g. Landi degl'Innocenti & Landolfi 2004). We set the central wavelength, the Doppler width and the Landé factor of the equivalent line to 650 nm, 1.6 km s<sup>-1</sup> and 1.25, respectively, and we adjust the average line-equivalent width to the observed value. Summing the spectral contributions of all grid cells yield the synthetic Stokes  $V$  profiles at a given rotation phase.

ZDI proceeds by iteratively comparing the synthetic profiles to the observed ones, until they match within the error bars. Since the inversion problem is ill-posed, ZDI uses the principles of maximum-entropy image reconstruction to retrieve the simplest image compatible with the data. The form we use for the regularization function is  $S = \sum_{l,m} l(\alpha_{l,m}^2 + \beta_{l,m}^2 + \gamma_{l,m}^2)$  (more details in Donati 2001).

ZDI depending on the assumed rotation period, it can be used to confirm and often to improve the accuracy of the estimate derived from  $B_l$  curves, as Stokes  $V$  profiles intrinsically contain more information than  $B_l$  curves. In some cases, surface differential rotation (DR) is required in order to fit Stokes  $V$  data down to the noise level. To achieve this, we assume that the rotation rate at the surface of the star depends on latitude and can be expressed as  $\Omega(\theta) = \Omega_{\text{eq}} - d\Omega \sin^2(\theta)$ , with  $\theta$  denoting the latitude,  $\Omega_{\text{eq}}$ , the rotation rate at the equator and  $d\Omega$ , the difference in rotation rate between the equator and the pole. This law is used to compute the phase shift of each ring of the grid at any observation epoch with respect to its position at a reference epoch. We carry out reconstructions for a range of  $\Omega_{\text{eq}}$  and  $d\Omega$  values; the optimum DR parameters are those minimizing the information content. They are obtained by fitting the surface of the  $\chi_r^2$  map with a paraboloid around the minimum value (Donati et al. 2003).

### 3.4 Results

The M dwarfs of our sample exhibit magnetic fields with Zeeman signatures that do not exceed 0.5% of the unpolarized continuum. We distinguish two kinds of magnetic topologies (see Table 5) : two stars harbour a large-scale magnetic field dominated by an axial dipole (GJ 358, GJ 205), whereas three stars exhibit a more complex field featuring a significant - in most case dominant - toroidal axisymmetric component (GJ 410, GJ 479 & GJ 846).

- GJ 358 & GJ 205 : For the stars whose large-scale field is mostly poloidal, the Stokes  $V$  LSD signatures are mainly anti-symmetric with respect to the line center. Their shape remain mostly constant (see, e.g., GJ 358 in Fig. 3), but their intensity vary significantly as the star rotates (see, e.g., the rotation cycles 0.235 and 0.789 in Fig. 3 top panel). For these stars, the reconstructed magnetic topologies are simple with more than 90% of the magnetic energy concentrated in a dipolar poloidal component (*i.e.*, SH mode with  $l = 1$ , see column 6 of Table 5). The Stokes  $V$  LSD signatures are fitted down to a  $\chi_r^2 \sim 1$ , from an initial value (corresponding to a null field map) of  $\sim 3.5$ -3.1 (depending on the S/N ratio and on the number of collected data). In the most magnetic regions, the flux reaches 230 G at the surface of GJ 358, but only 30 G at the surface of GJ 205 (see Fig. D1).

- GJ 479 & GJ 410 : For the stars with a significant toroidal component, the Stokes  $V$  LSD profiles have a sign that varies dur-

Nom	$M_\star$ ( $M_\odot$ )	$P_{\text{rot}}$ (d)	$B_V$ (G)	Pol. (%)	Dip. (%)	Axi (%)
GJ 205	0.61	$33.63 \pm 0.37$	20	99	90	73
GJ 358	0.41	$25.37 \pm 0.32$	130	97	98	85
GJ 410	0.58	$13.83 \pm 0.10$	65	25	88	11
GJ 479	0.43	$24.04 \pm 0.75$	65	37	74	29
GJ 846 (#1)	0.59	$10.73 \pm 0.10$	45	27	69	68
GJ 846 (#2)	0.59	$10.73 \pm 0.10$	30	63	52	86

**Table 5.** Properties of the large-scale magnetic field topologies of the moderately active M dwarfs sample. In columns 1-3 we report the name of the star (with runs #1 and #2 for GJ 846 corresponding to the first and second observing epochs, see Table B4), the mass and the rotation period, initially presented in Table 1. Column 4 mentions the assessment of the average magnetic flux reconstructed from the Zeeman signatures. Column 5 lists the magnetic energy lying in poloidal component. Columns 6-7 present the magnetic energy reconstructed as a poloidal dipole and the percentage of poloidal energy in axisymmetric modes (defined as  $m < l/2$ ).

ing the stellar rotation (see, e.g., the rotation cycles 2.067 and 2.493 of GJ 410 in Fig. 4 top left panel). The large-scale magnetic field reconstruction indicates that the axisymmetric poloidal component includes less than 40% of the magnetic energy (see column 7 of Table 5), and features a mostly dipolar structure ; the toroidal component includes more than 60% of the reconstructed magnetic energy, and is mostly axisymmetric, showing up as an azimuthal field ring of  $\sim 80$  G encircling the star at equatorial or intermediate latitudes (see Table 5, two last rows, and Fig. 4 and Fig. D2 bottom panel, for, resp., GJ 410 and GJ 479). The magnetic field flux is moderate, reaching  $\sim 70$  G in the in the strongest field regions.

Moreover, thanks to the dense spectropolarimetric data set of GJ 410 (42 measurements spread over 7.5 rotation cycles), we can easily estimate the amount of latitudinal DR shearing the magnetic maps. Indeed, the Stokes  $V$  LSD data set of all stars of our sample can be fitted down to  $\chi_r^2 = 1$  when assuming solid body rotation, except for GJ 410 ( $\chi_r^2 = 1.6$ ). Assuming DR, we are able to fit the data of this early-M dwarf down to  $\chi_r^2 = 1.0$ , with  $\Omega_{\text{eq}} = 0.47 \pm 0.03$  rad d<sup>-1</sup> and  $d\Omega = 0.05 \pm 0.03$  rad d<sup>-1</sup> (see Fig. 5), corresponding to rotation periods at the equator and pole of  $13.37 \pm 0.86$  and  $14.96 \pm 1.25$  d, respectively. This result is in good agreement with  $P_{\text{rot}}$  previously found ( $13.83 \pm 0.10$  d, Sec. 3.2), and with the former DR estimate of GJ 410 (see Donati et al. 2008).

Finally, we note that the large-scale field of GJ 410 significantly evolved between 2007-2008 (Donati et al. 2008) and 2014 (our data), both in strength (decreasing from 100 to 60 G) and in topology (the energy in the dipolar component increased from 50 to 88%).

- GJ 846 : For GJ 846, we notice a variability of the large-scale magnetic topology between 2013 and 2014, as expected from the  $B_l$  analysis (Sec. 3.2). More specifically, the energy in the poloidal component increases from 27% in 2013 to 63% in 2014 (see Fig. D3, middle and bottom panels),

Early-M dwarfs like GJ 410 and GJ 846 were already reported to be prone to increased variability, probably as a result of their stronger surface differential rotation (see Morin et al. 2008a,b; Donati et al. 2008).

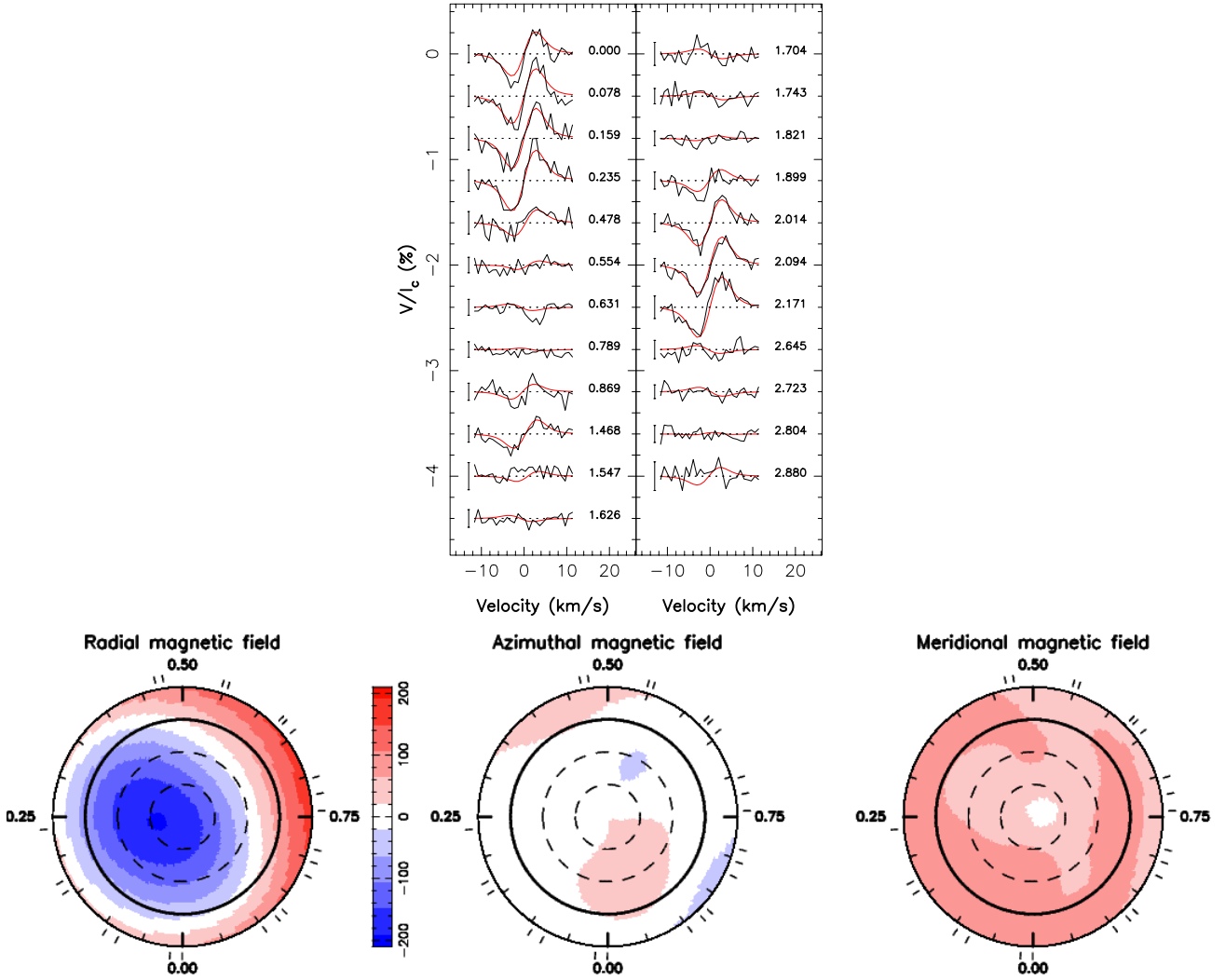


**Figure 3.** *Top:* maximum-entropy fit (thin red line) to the observed (thick black line) Stokes  $V$  LSD photospheric profiles of GJ 358. Rotational cycles and  $3\sigma$  error bars are also shown next to each profile. *Bottom:* map of the large-scale magnetic field at the surface of GJ 358. The radial (left corner), azimuthal (center) and meridional (right corner) components of the magnetic field  $B$  are shown. Magnetic fluxes are labelled in G. The star is shown in a flattened polar projection down to latitude  $-30^\circ$ , with the equator depicted as a bold circle and parallels as dashed circles. Radial ticks around each plot indicate phases of observations. This figure is best viewed in color.

#### 4 CHARACTERIZATION OF THE RV JITTER

Our sample stars are known to exhibit RV variations caused by stellar activity. To characterize the origin of the RV modulation, we compute the bisector, the full width at half-maximum FWHM, and the  $H\alpha$  index as described in section 4.1. We then analyse how these quantities vary with time through their Lomb-Scargle periodograms, and compare with temporal variations of the RV itself (see Sec. 4.2.1). As the model we propose aims at modeling the component of the RV signal that is rotationally modulated (see Sec. 5), the first step is to assess quantitatively the amount to which the RVs of our sample stars are periodic (see Sec. 4.2.2).

##### 4.1 Computing RVs and activity proxies

RVs are computed by fitting a Gaussian to the Stokes  $I$  LSD profiles (equivalent to the CCF), the Gaussian centroid giving the RV estimate  $v_r$ . The FWHM measurements is directly computed from the Gaussian fit to the Stokes  $I$  LSD profiles.

To derive the bisector, we first interpolate the CCF profile using a cubic spline interpolation; we then compute the set of midpoints of horizontal line segments extending across the profile (Gray 1982). To assess temporal evolution of the line profile, we calculate the velocity span (as introduced, e.g., by Gray 1982; Queloz et al. 2001)  $v_s$ , given by  $v_t - v_b$ , where  $v_t$  and  $v_b$  are respectively the average velocity at the top and bottom parts of the bisector<sup>3</sup>. For RV variations caused by stellar activity, we commonly observe an anti-correlation between  $v_s$  and  $v_r$  (see, e.g., Queloz et al. 2001). However, as expected for slow rotators whose rotation profile is not resolved by the velocimeter (typically  $v \sin i < 2 \text{ km s}^{-1}$ , see e.g., Desort et al. 2007), this  $v_s$  vs.  $v_r$  anti-correlation is not observed in our sample,  $v_s$  exhibiting no variations (for example, for GJ 358,  $v_s$  has a peak-to-peak amplitude of  $\sim 10 \text{ m s}^{-1}$  and a rms of  $3.6 \text{ m s}^{-1}$ , see Fig. 6). For this reason, this proxy is not discussed in

<sup>3</sup> The top and bottom parts include all points within 10-40% and 60-90% of the full line depth, respectively.

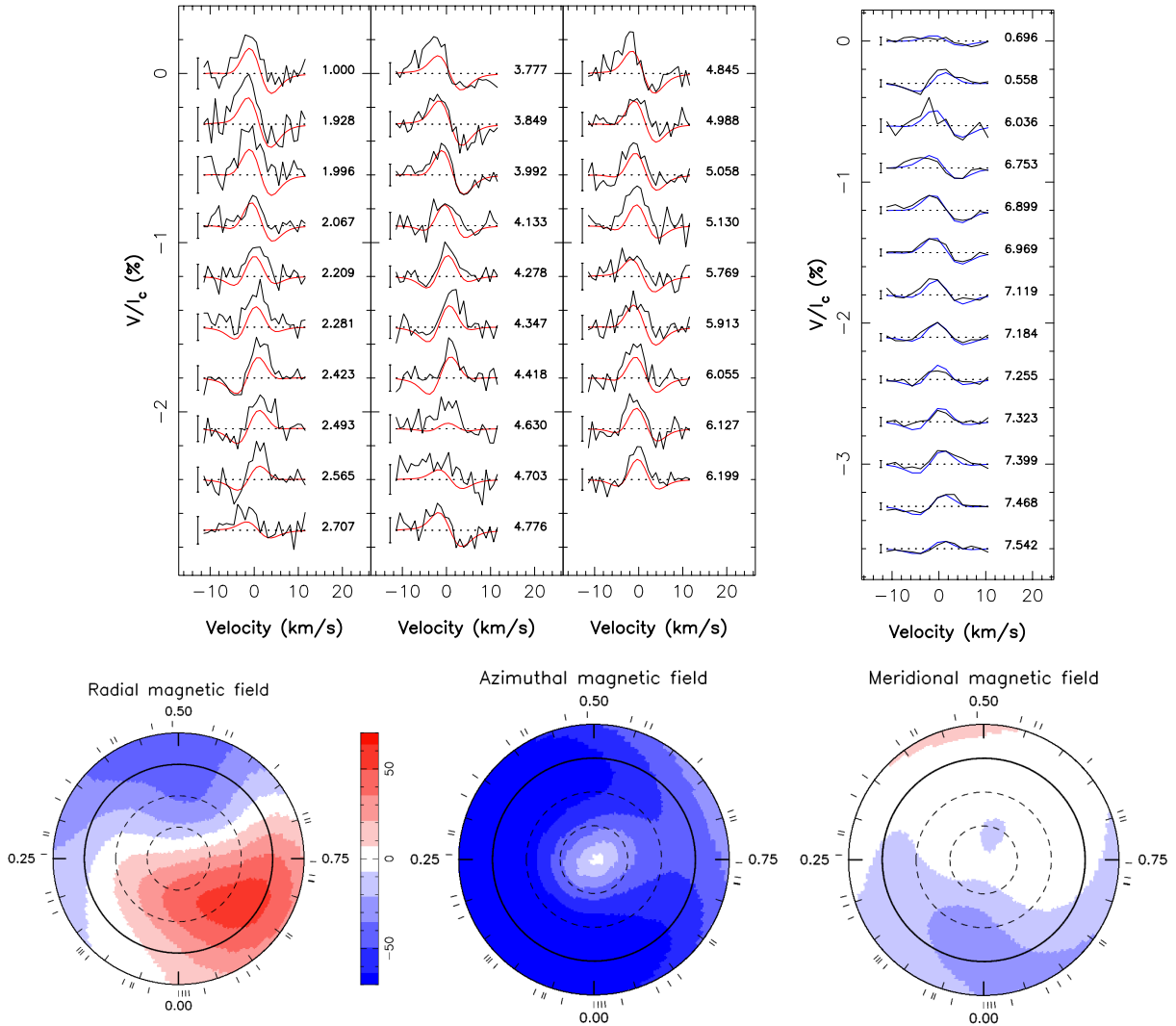


**Figure 4.** Same as Fig. 3 for GJ 410. LSD Stokes  $V$  profiles in the top left and top right panels correspond to HARPS-Pol and NARVAL observations respectively.

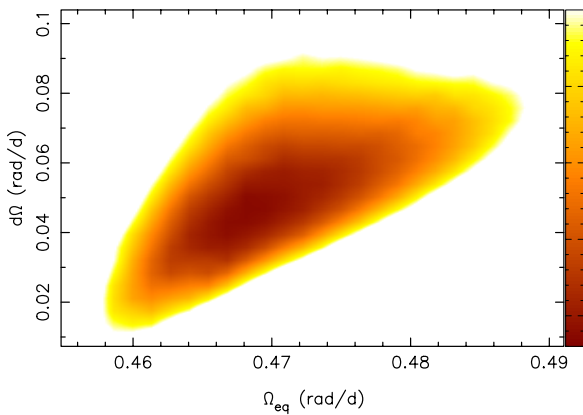


**Figure 5.** Variations of  $\chi_r^2$  as a function of  $\Omega_{eq}$  and  $d\Omega$ , derived from the modelling of GJ 410 Stokes  $V$  LSD profiles at constant information content. The outer colour contour traces the 1.75% increase in  $\chi_r^2$  that corresponds to a  $3\sigma$  ellipse for both parameters as a pair.

the following sections, even though  $v_s$  is computed and shown on Fig. 6 and similar following graphs.

The  $H\alpha$  index is also often used to characterize RV variations caused by activity. This index is defined as the ratio between the flux in the  $H\alpha$  absorption line and that in the surrounding continuum, as described in Boisse et al. (2011). We use a 0.16 nm window centered at 656.2808 nm for the central line, and two windows of 1.075 and 0.875 nm around 655.087 and 658.031 nm respectively for the continuum as presented in Gomes Da Silva et al. (2011).

## 4.2 Activity jitter in the M dwarfs sample

### 4.2.1 Diagnostic of the activity

Only 11 RV measurements spanning 5.4 rotation cycles were collected for GJ 846 (run #2) - too sparse a set for a reliable periodogram analysis. As a result, the following sections concentrate only on the 4 other stars of the sample, namely GJ 358, GJ 479, GJ 410 and GJ 205.

- GJ 358 : The  $B_I$ , RV, FWHM,  $H\alpha$  and  $v_s$  curves as well



as the periodograms of  $B_l$ , RV, FWHM and  $H\alpha$  are presented in Fig. 6. The periodograms of both  $H\alpha$  and FWHM show that the period  $P_{\text{rot}}$  previously identified with  $B_l$  has significantly more power than its harmonics (FAP < 1% for FWHM, < 15% for  $H\alpha$ ). It is a further confirmation that the observed RV modulation is mainly caused by activity. The periodogram of  $v_r$  indicates a period of  $P = 24.47 \pm 0.60$  d, in agreement with  $P_{\text{rot}}$ , but with a FAP of only 10%. Moreover, we notice that  $v_r$  and  $B_l$  vary in quadrature : when  $B_l$  reaches its maximum value (of about +10 G),  $v_r$  is at mid-distance between its maximum and minimum (see, *e.g.*, phases 0.70-0.75).

- GJ 479 :  $H\alpha$  and FWHM show variations with a period in the range 23-25 d, in agreement with the  $P_{\text{rot}}$  that we previously derived from our  $B_l$  data. RVs allows to measure a period of  $23.2 \pm 1.9$  d, again fully compatible with  $P_{\text{rot}}$  (see Fig. E1). Moreover the  $H\alpha$  periodogram exhibits a similar harmonics spectrum (from  $P_{\text{rot}}$  to  $P_{\text{rot}}/4$ ) as those of  $B_l$  and  $v_r$ . Furthermore the shape of  $v_r$  and  $B_l$  curve are very similar, in particular  $v_r$  crosses its median value when  $B_l$  is close to zero (see, *e.g.*, phase 0.45).

- GJ 410 : Being the most active star of our sample, GJ 410 exhibits the largest temporal variations for all proxies (typically  $\times 1.5$ , see Fig. 7). The periodogram of  $v_r$  indicates a period  $P = 14.20 \pm 0.20$  d, within the range of surface periods that differential rotation triggers (13.4-15.3 d, see Sec. 3.4). The period measured with  $v_r$  being higher than  $P_{\text{rot}}$  measured with  $B_l$ , this suggests that the surface spots generating the observed RV variations are located at mid to high latitudes.

- GJ 205 : The data and their periodograms are presented in Fig. E2. The  $H\alpha$  periodogram shows a main peak at 33.46 d with a FAP  $\leq 15\%$ . This period is consistent with the  $P_{\text{rot}}$  derived from  $B_l$  and mentioned in Kiraga & Stepien (2007) (33.63  $\pm$  0.37 d and 33.61 d resp.), and confirms that the observed signals are due to stellar activity. FWHM measurements do not allow to firmly identify the rotation period of the star, and no signal with the  $P_{\text{rot}}$  derived from  $B_l$  is detected in  $v_r$  with a FAP of 98%. The strongest peak in  $v_r$  periodogram is at  $39.70 \pm 0.85$  d and not compatible with  $P_{\text{rot}}$ . However, GJ 205 being an early-M dwarf, one can assume that it features a similar amount of DR to that observed on GJ 410, *i.e.*,  $d\Omega = 0.05 \text{ rad d}^{-1}$ . This level of differential rotation would correspond to a difference of 10 d between the polar and the equatorial rotation periods, and would thus allow to reconcile the observed peaks in the different periodograms. If confirmed, this would suggest that dark spots are located at high latitudes. Unfortunately, the present data set does not allow to measure the DR, and to further confirm this assumption.

Comparing the period derived from  $B_l$  and those derived from RV, FWHM and  $H\alpha$  (see Table A1) demonstrates that the rotation period of the star is most of the time more efficiently determined through  $B_l$  data than through RVs or other usual activity proxies (high FAP). In our small sample, we find that the different period values are in agreement for GJ 358 and GJ 479. We thus can suspect a solid rotation and/or that the strongest magnetic area and the spots are at similar latitudes. For GJ 410, the periods differ but are in agreement with the differential rotation we measured from the magnetic data. Finally, for GJ 205, we suspect a differential rotation effect, but we cannot measure with the current dataset.

This preliminary analysis demonstrates that most of our sample stars show rotationally modulated RVs, whose variations are

obviously linked with those of the longitudinal field and other activity proxies. By comparing these different values of period, we can thus further investigate the origin of the observed RV jitter.

#### 4.2.2 RV signal detection

The rms of the data ( $\text{rms}_0$ ) is 2-3 $\times$  higher than the average noise  $\sigma_0$ . The multiple sine fit (including the two first harmonics) to the RV data allows to improve  $\chi_r^2$  with respect to a fit with a constant RV, however we never reach  $\chi_r^2 = 1.0$  (see Table 6, 7 first columns). This suggests that the RV jitter,  $J_{\text{rot}}$ , includes both a rotationally modulated component  $J_m$  (due, *e.g.*, to long-lived spots at the stellar surface), as well as a randomly varying one  $J_r$  (of yet unclear origin, *e.g.*, spots with lifetimes shorter than the rotation cycle). Their respective strengths vary from one star to the other. For example, the poorest fit to the data are that of GJ 205, whose period in the RV data significantly differs from  $P_{\text{rot}}$  (determined from the magnetic data, see Sec. 3.2) and for which periodicity in the  $v_r$  signal is not really detected.

Multiple sine fits and Doppler-imaging (see Sec. 5) can only succeed at modeling signals varying periodically with  $P_{\text{rot}}$ ; our first task is thus to quantify the extent to which the observed RV signals are indeed mostly modulated by rotation. We thus compute the probability that a multiple sine fit provides a significantly better match to the observed RV variations than does a constant RV. We use the incomplete Gamma function to assess this probability  $p$ , given both the number of degrees of freedom and the improvement in  $\chi_r^2$  that a multiple sine fit (including 2 harmonics) provides with respect to a constant RV. The closer  $p$  gets to 1.0 and the false alarm probability (FAP = 1- $p$ ) to 0, the more reliably the rotational modulation of the RV signal is detected and dominates the RV variations. As we test the ability of the model to fit the rotationally modulated component  $J_m$ , we use a scaled  $\Delta\chi^2$  given by:

$$\Delta\chi^2 = \frac{\chi_{r,0}^2 - \chi_{r,1}^2}{\chi_{r,1}^2} \cdot N, \quad (3)$$

where N denotes the number of measurements. The resulting FAP are gathered in Table 6. We note that for GJ 358, GJ 479 and GJ 410,  $J_m$  is dominant with a FAP level of < 1%, whereas for GJ 205  $J_r$  largely dominates the signal (with a FAP level of  $\sim 73\%^4$ ), so that for this star no coherent signal is detected at the rotation period measured from  $B_l$ .

To quantify the strength of  $J_m$  and  $J_r$ , we compute their rms, once having quadratically subtracted the noise (see Table 7). Whereas  $J_m$  is the major component for GJ 358 and, in a smaller extend for GJ 479, the trend is reversed for GJ 205 and GJ 410, where  $J_r$  becomes dominant. The Doppler imaging being able to model the rotational modulation only, we aim at reduce the activity jitter by a factor  $A_1$ .

## 5 MODELING OF THE RV JITTER

The goal of this section is to consistently model the rotationally modulated component of the activity jitter (called  $J_m$  in Sec. 4.2.2)

<sup>4</sup> However if we assume that DR is present at the surface of GJ 205 (at a level similar to that reported for GJ 410) and is responsible for modulating the RV data with a period of  $39.70 \pm 0.35$  d (rather than that of  $33.63 \pm 0.37$  d derived from the magnetic data), the FAP level drops down to 2%.

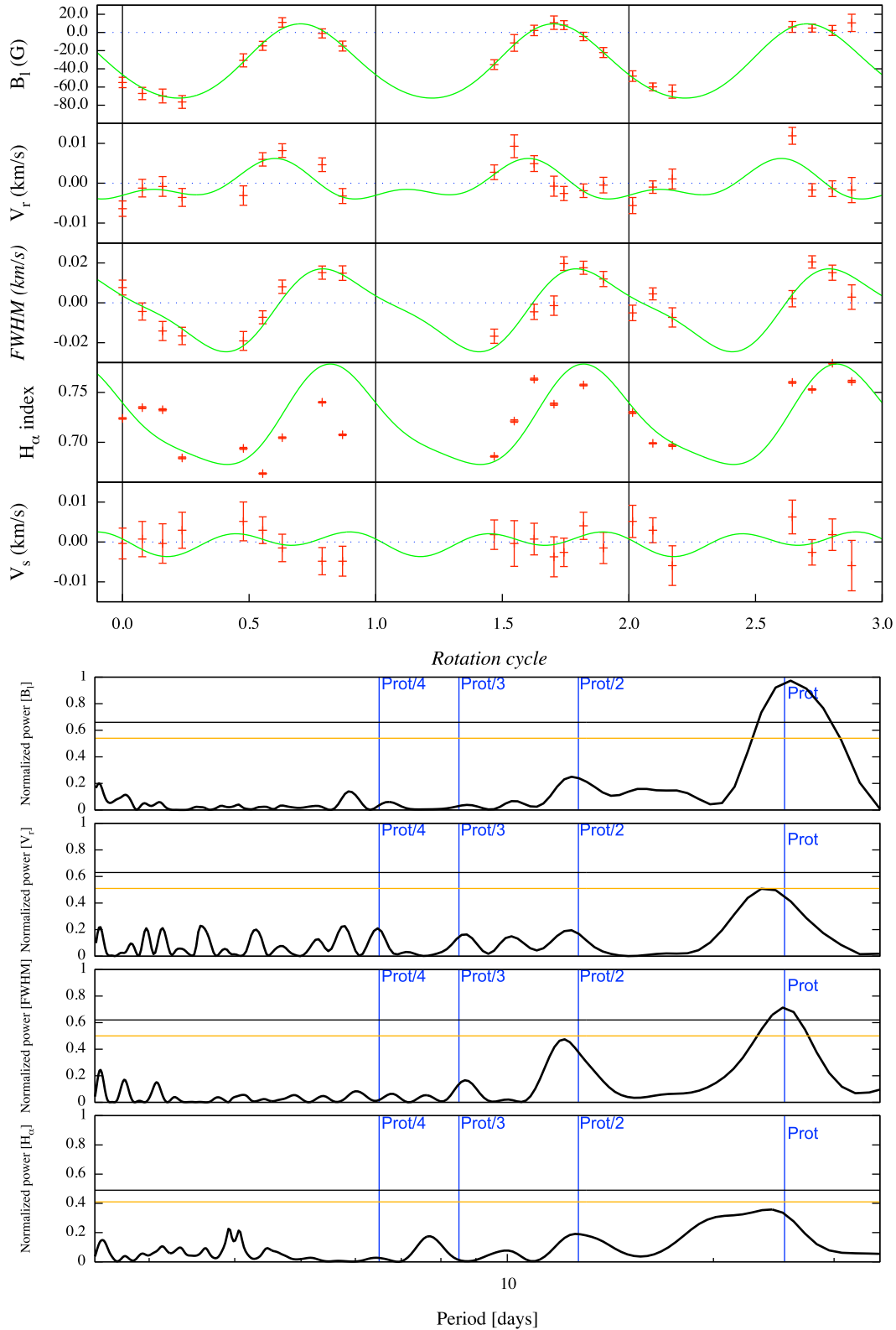


**Figure 6.** *Top:* Temporal variations of  $B_l$ ,  $v_r$ , FWHM,  $H_\alpha$  and  $v_s$  for GJ 358. Data and their error bars are in red. For all plots, the zero level is depicted by a dotted line. The green lines depict a multiple sine fit (including the fundamental at  $P_{rot}$  and first harmonic at  $P_{rot}/2$ ) to the data points. The vertical black lines outline the beginning of each rotation cycle. *Bottom:* Lomb-Scargle periodograms of  $B_l$ ,  $v_r$ , FWHM and  $H_\alpha$  for GJ 358. The blue vertical lines outline the rotation period  $P_{rot}$  and its first 3 harmonics at  $P_{rot}/2$ ,  $P_{rot}/3$  and  $P_{rot}/4$ . The yellow and black horizontal lines respectively mark FAP levels of 10% and 1%.

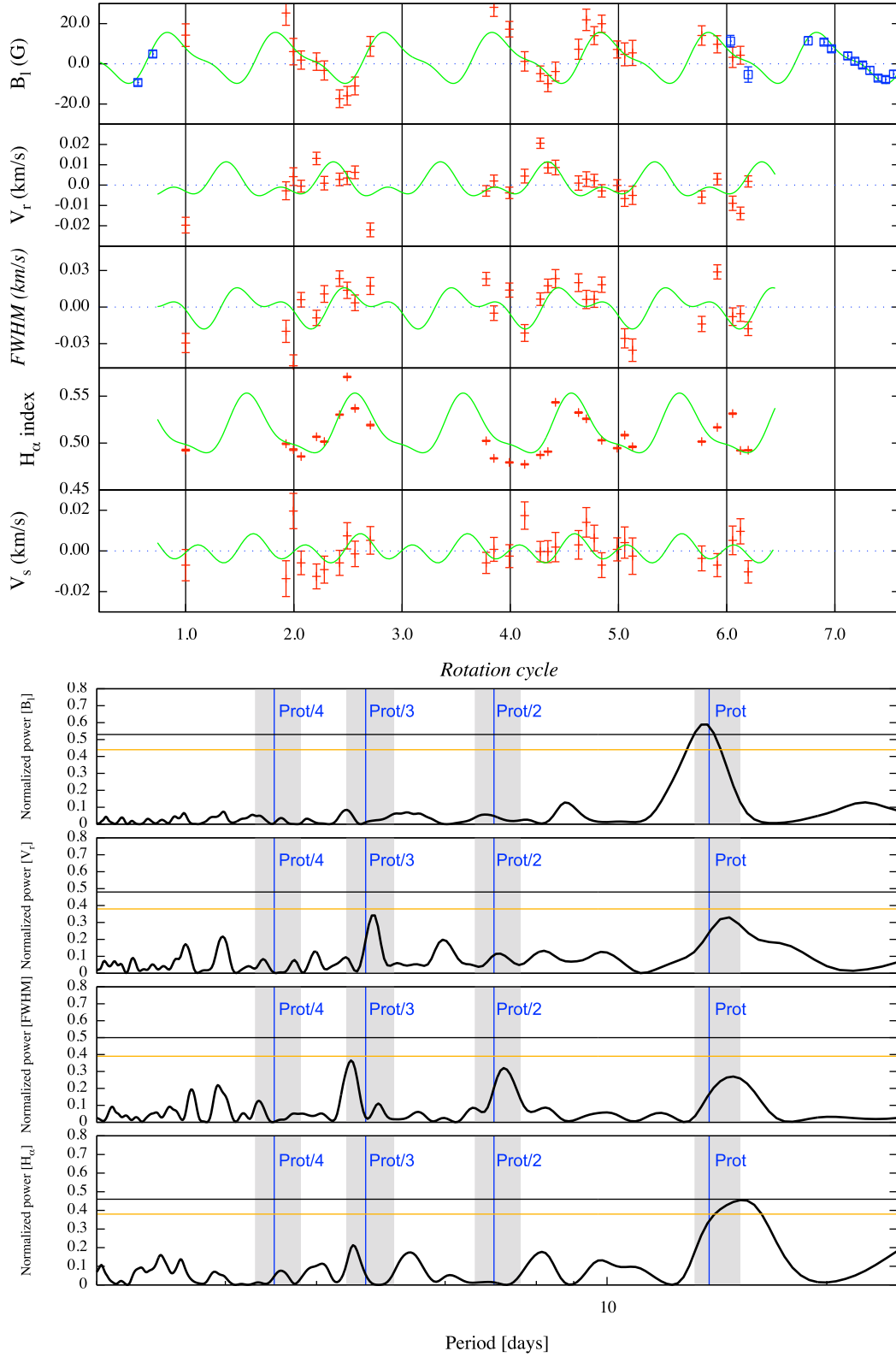


**Figure 7.** As Figure E1 for GJ 410. The blue data are the  $B_l$  values computed from NARVAL LSD profiles. The grey bands depict the range of periods at the surface of the star as a result of DR.

	Raw RV data		Multiple sine fit (fond. + 2 harm.)				DI modeling					
	$\sigma_0$	rms <sub>0</sub>	$\chi_{r,0}^2$	rms <sub>1</sub>	$\chi_{r,1}^2$	FAP	RV curve			LSD profiles		
	(m s <sup>-1</sup> )	(m s <sup>-1</sup> )		(m s <sup>-1</sup> )		(%)	rms <sub>2</sub>	$\chi_{r,2}^2$	FAP	$\chi_{r,i}^2$	$\chi_{r,f}^2$	FAP
GJ 205	1.45	3.52	7.81	3.05	6.27	73	3.17	6.31	98	4.3	3.8	75
GJ 410	3.28	8.84	7.85	6.55	3.96	0.04	6.78	4.14	2.8	2.9	2.0	≤ 0.01
GJ 479	2.02	5.29	7.71	3.65	3.58	0.09	3.93	4.05	7.4	5.0	2.9	≤ 0.01
GJ 358	2.08	4.79	5.59	2.47	1.69	≤ 0.01	2.88	2.05	≤ 0.01	3.8	2.1	≤ 0.01

**Table 6.** Table of the parameter that characterize the detection and the multiple sine fit of the RV activity jitter. The first column gives the name of the star, columns 2-4 give the observed average RV noise  $\sigma_0$ , the rms of the RV data rms<sub>0</sub>, and the associated  $\chi_{r,0}^2$ . Columns 5-6 mention the rms of the RV residual obtained after a multiple sine-fit (fundamental + 2 harmonics), the  $\chi_r^2$  associated to the fit  $\chi_{r,1}^2$ . Column 7 lists the estimate of the likelihood of the fit (FAP, see text). Columns 8-10 give the rms of the RV residuals after the DI modeling, the associated  $\chi_r^2$ , and the FAP. Columns 11-13 list the initial and final  $\chi_r^2$  linked to the *RI* reconstruction, and the associated FAP.

	$J_{\text{tot}}$	$J_m$	$J_r$	$A_1$
	(m s <sup>-1</sup> )	(m s <sup>-1</sup> )	(m s <sup>-1</sup> )	
GJ 205	3.21	1.75	2.68	1.2
GJ 410	8.21	5.67	5.93	1.4
GJ 479	4.89	3.83	3.04	1.7
GJ 358	4.31	4.10	1.33	3.2

**Table 7.** The first column indicates the name of the star. Column 2 gives rms<sub>*J*,tot</sub>, the rms of the RV data, once the noise has been quadratically subtracted ( $J_{\text{tot}} = \sqrt{\text{rms}_0^2 - \sigma_0^2}$ , with rms<sub>0</sub>, the rms of the data, see Table 6). Column 3 mentions  $J_m$ , the rms of the RV jitter due to rotational modulation ( $J_m = \sqrt{\text{rms}_0^2 - \text{rms}_1^2}$ ). Column 4 indicates the rms of the random component of the RV jitter,  $J_r$  ( $J_r = \sqrt{\text{rms}_1^2 - \sigma_0^2}$ ). With a model of the rotational modulation only, we can reduce the activity jitter by a factor  $A_1 = J_{\text{tot}}/J_r$  (column 5).

and translate it into a distribution of surface features, whose relation to the parent magnetic topology (described in Sec. 3.4) can be studied - at least on a statistical point of view.

For this first approach, we assume that the distortions observed in Stokes *I* LSD profiles are only due to rotational modulation induced by spots. On the stellar surface, two kinds of features can be found: hot/bright plagues and cool/dark spots. These features induce a RV activity jitter and variations of the bisector span. When the contribution of spots is dominant, the amplitude of the RV variations is higher than those of the bisector span, and when the contribution of plagues is dominant, the amplitude of the RV variations is similar to or smaller than those of the bisector span (Dumusque et al. 2014, Eq.10). In our sample,  $v_s$  data do not exhibit a peak-to-peak amplitude higher than 15 m s<sup>-1</sup> and we do not observe any clear  $v_s$  variations (see Sec.4.1), whereas the peak-to-peak amplitude of RV variations is always higher than 15 m s<sup>-1</sup>. Moreover, thanks to 3D-simulations of the near-surface convection of M dwarfs that take into account the small-scale magnetic field, Beeck et al. (2015) show that dark spots are much more abundant than plagues. Thus, at first order, we consider dark spots only as the main origin of the observed rotationally modulated RV variations.

In the imaging procedure, we characterize a spot with its relative brightness *b*, and its local profile  $I_s$ . This two parameters being fixed, we adopt a simple two-temperature model (warm photosphere, cool spots) for the stellar surface and we choose the spot covering fraction as image parameter.

## 5.1 Method

As previously presented for the magnetic field reconstruction, the stellar surface is divided into 5000 cells, and the Stokes *I* profile at a given rotation phase is computed as the sum of all local Stokes *I* profiles from the different cells. With the spot description we chose, the parameter we reconstruct during the ZDI process is  $1 - C_j$ , with  $C_j$  denoting the proportion of photosphere inside each cell ( $C_j = 0$  and  $C_j = 1$ , respectively, corresponding to a spotted cell, and to an unspotted cell), and therefore, the local profile  $I_j$  of the cell *j* is given by :

$$I_j = C_j I_p + b(1 - C_j) I_s \quad (4)$$

where  $I_p$  is the local unpolarized profile within the photosphere,  $I_s$  that within the spot, and *b* the relative spot to photosphere brightness contrast. To compute  $I_p$ , we use the profile given by UR's analytical solution of the polarized radiative transfer equation in a Milne Eddington's atmosphere (see Hébrard et al. 2014 for the values of the different parameters) and we adjust the average line-equivalent width to the observed value only. Following Dumusque et al. (2014), the local profile within the spot  $I_s$  is simply a broadened version (by a Gaussian of FWHM  $w = 2-3$  km s<sup>-1</sup>, depending on the stars) of that in the photosphere  $I_p$ . We also have the option of red shifting  $I_s$  with respect to  $I_p$  (to simulate the inhibition of the convective blue shift within the spot). However, we did not use this option for the present study given that convective blue shifts of M dwarfs are expected to be quite small.

As a result of their low  $v \sin i$ , our sample stars feature spectral lines that mostly reflect their intrinsic profiles rather than their Doppler broadening (as opposed with most stars studied to date with conventional Doppler imaging, e.g., Collier Cameron 1992; Morin et al. 2008a). The consequence is that a direct modeling of the observed profiles would critically depend on our ability to achieve a detailed description of the local profile.

To overcome this limitation, we propose a novel technique, based on interpreting the residuals with respect to the average profile, rather than the profiles themselves. Practically speaking, we start the process by computing the average profile over the whole data set  $\langle I \rangle$ . We then subtract  $\langle I \rangle$  from each individual Stokes *I* profile of the time series to derive the profile residuals *RI* that directly reflect the profile distortions and include most information about the spot distribution to be reconstructed. In parallel, we model  $\langle I \rangle$  by adjusting the parameters of the local profile  $I_p$  until we obtain a good fit (including the Doppler broadening); we call

this model average profile  $\langle I' \rangle$ . We then sum the  $RI$  residuals to  $\langle I' \rangle$  and obtain a new data set  $I'$ . Since  $\langle I' \rangle$  is now perfectly known, the imaging code can concentrate its efforts on reproducing the  $RI$  residuals, i.e. the core material of our data set.

## 5.2 Simulations

We performed a set of simulations to test the performances of our novel reconstruction method. From an initial brightness map, we compute the associated Stokes  $I$  and  $RI$  data set for a given  $v \sin i$ , stellar inclination  $i$ , and spectral resolution. The objective is to retrieve both the brightness map and the quantities derived from the reconstructed profiles : the RV curve  $v_r$ , FWHM and  $v_s$ .

We present below the simulation results obtained in the case of slow rotators ( $v \sin i \leq 4 \text{ km s}^{-1}$ ), and derived assuming a spectral resolving power of  $10^5$  (i.e., the resolution of HARPS-Pol). We further assume that the S/N of the LSD profile residuals  $RI$  is equal to 4,000 (value close to the observed S/N). Two different cases are studied : (i) a dense and regular sampling to test more specifically the use of the residuals (simulation A), and (ii) irregular sampling based on the observation of GJ 479, to mainly estimate the impact of a realistic phase coverage on the determination of the average profile (simulation B).

Dark spots are assumed to be circular with a relative size  $f^5$  with respect to the overall stellar surface. The total equivalent spot area,  $\epsilon$ , is thus defined as  $\epsilon = f \times (1 - C) \times b$ . For our simulation, we set  $b = 0.5$ . We consider two dark spots : spot #1 has a relative area of  $f_1 = 3\%$  with  $C_1 = 0.4$  and thus  $\epsilon_1 = 0.9\%$ , and is located at  $20^\circ$  of latitude, spot #2 is characterized by  $f_2 = 1.5\%$  with  $C_2 = 0.2$ , and thus  $\epsilon_2 = 0.6\%$ , and is at  $50^\circ$  of latitude. The full equivalent spot area  $\epsilon$  is equal to  $\epsilon_1 + \epsilon_2 = 1.5\%$ . The  $v \sin i$  of the star ranges from 1 to  $4 \text{ km s}^{-1}$ , and the stellar inclination is  $i = 60^\circ$ . The local profile within a spot is 15% larger than in the quiet photosphere.

### 5.2.1 Reconstructed map

Figure 8 (top part) and Table 8 show, respectively, the maps and their associated reconstructed characteristics. To test the impact of using the profile residuals  $RI$  instead of Stokes  $I$ , we compare the maps obtained using Stokes  $I$  profiles directly (called hereafter 'the conventional method') with those obtained from the  $I'$  replacement data set described above (called below 'the residual method').

We note that the global spot distribution is recovered, whatever the technique we used. With the conventional method,  $\chi_r^2 = 1.0$  is reached whatever the  $v \sin i$  and the phase coverage. However the spotted area is roughly under-estimated with decreasing  $v \sin i$ . A similar but amplified behavior is observed with the residual method. The use of the average profile  $\langle I \rangle$  to compute the  $I'$  dataset mainly affects the reconstructed spotted equivalent spot coverage  $\epsilon$ , which ends up being underestimated (1.25-1.45% instead of 1.5% depending on the  $v \sin i$ ). This loss of accuracy when  $v \sin i$  decreases mainly reflects that information gets increasingly blurred in longitude as stellar rotation slows down, thus weakening profile distortions and making them harder to reconstruct for the code.

<sup>5</sup> defined as the fractional area of the star covered by a spot,  $\frac{1 - \cos \alpha}{2}$ , see Hébrard et al. (2014)

simu	$v \sin i$ (km s <sup>-1</sup> )	initial $\chi_r^2$	final $\chi_r^2$	spotted area (%)
Imaging from $I$ = conventional method				
A	1	6.5	1.0	1.35
	2	12.2	1.0	1.45
	4	24.9	1.0	1.50
B	1	4.7	1.0	1.30
	2	8.1	1.0	1.45
	4	17.4	1.0	1.50
Imaging from $I'$ = residual method				
A	1	4.7	1.13	1.35
	2	11.5	1.11	1.40
	4	24.7	1.0	1.50
B	1	3.3	1.15	1.25
	2	8.2	1.1	1.40
	4	18.0	1.0	1.45

**Table 8.** Parameters of the reconstructed map for a star with  $v \sin i = 1 \text{ km s}^{-1}$  and  $i = 60^\circ$  with 2 spots covering 1.5% of the stellar surface. Column 1 gives the considered simulations, and column 2 the  $v \sin i$  of the stars. Columns 3-4 indicates the initial and final  $\chi_r^2$  associated with the reconstruction. Column 5 give the spotted reconstructed area. The results obtained from imaging using directly  $I$  are given in black, the results obtained from  $RI$  are given in blue. Simulation A : reconstruction from a dense and regular sampling. Simulation B : reconstruction from a random sampling.

Simu	$v \sin i$ (km s <sup>-1</sup> )	(m s <sup>-1</sup> )						
		(a)	(b)	(c)	(d)	(e)	(f)	(g)
A	1	1.5	2.0	2.4	4.9	1.6	1.5	12.9
	2	1.7	2.4	2.4	10.4	2.1	1.5	11.9
	4	2.9	3.2	3.2	25.3	6.3	2.8	27.3
B	1	1.6	1.8	2.1	3.6	1.7	1.4	17.7
	2	1.8	1.8	2.1	8.3	2.0	1.2	13.4
	4	3.2	3.2	3.3	18.5	4.6	2.6	31.3

**Table 9.** Column 1 gives the studied simulation, column 2 the  $v \sin i$  of the star. Column 3 indicates the rms RV noise, whose increase with  $v \sin i$  reflects the decrease in RV precision resulting from the shallower and broader line profiles of faster rotators. Columns 4-9 give the rms of the RV residual, after a filtering from the direct method (b), from the indirect method (c), from a multiple sine-fit with, respectively, 1, 2 and 3 harmonics (d)-(f) , and from the anti-correlation  $v_r - v_s$  (g) .

### 5.2.2 Model of the RV jitter

The main parameter we aim at recovering is the RV curve shown in Figure 8 (3rd row, on the left) in the case of  $v \sin i = 1 \text{ km s}^{-1}$ .

First, we note that RV variations are fitted down to the noise level, with both methods. For this spot configuration, the periodogram exhibits conspicuous peaks at  $P_{\text{rot}}$  and  $P_{\text{rot}}/2$ . We find that both imaging methods provide similar results in the sense that they are quite successful at filtering the rotationally modulated activity jitter; we do not observe any strong peaks in the periodogram of the RV residuals O-C (= observed - computed, see periodograms Figure 8, right bottom panel).

To quantify the model efficiency, we compare the rms of O-C

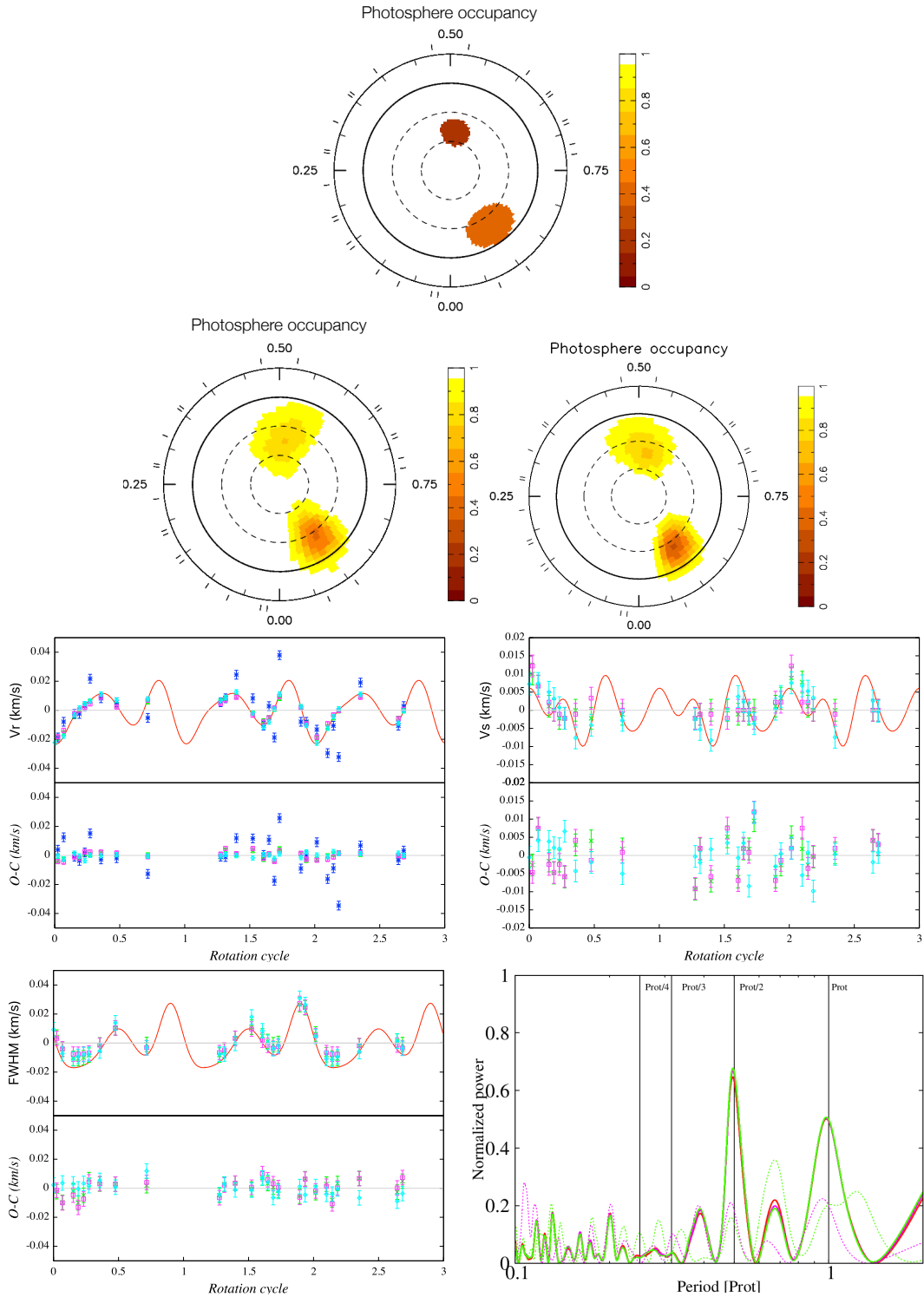


**Figure 8.** Reconstructed map obtained for a simulated star with  $v \sin i = 1 \text{ km s}^{-1}$  and  $i = 60^\circ$  featuring an equivalent spot area  $\epsilon$  of 1.5%. *Top:* Spot distribution to reconstruct. *2nd row, left:* Reconstructed map from  $I$  with the realistic sampling  $B$ . *2nd row, right:* Same as *left* but reconstructed from RI residuals. The colour-scale depicts the photosphere filling factor of each cell  $C_j$  (white corresponding to an unspotted cell). *3rd row, left:* original  $v_r$ 's (red solid line) compared with those reconstructed using either the conventional (pink open squares) or residual (green crosses) imaging method respectively, and with those derived from the  $v_r$ - $v_s$  anticorrelation (blue asterisks). The multiple sine fit to the data (cyan open diamonds) is also shown. The corresponding O-C residuals are presented on the bottom curve. The gray line depicts the  $0 \text{ m s}^{-1}$  level. *3rd row, right:* Same as *3rd row, left* but for  $v_s$ . *Bottom left:* Same as *3rd row, left* but for FWHM. *Bottom right:* Periodograms of  $v_r$  (solid red line), of the  $v_r$  computed from data set obtained with the conventional method (solid pink line), and with the residual method (solid green line). The periodograms of the filtered RVs (using either the conventional or the residual method) are respectively shown with the red and green dashed lines. The vertical lines outline the rotation period (in unit of  $P_{\text{rot}}$ ) and its 3 first harmonics ( $P_{\text{rot}}/4$ ,  $P_{\text{rot}}/3$ ,  $P_{\text{rot}}/2$ ). This figure is best viewed in colour.

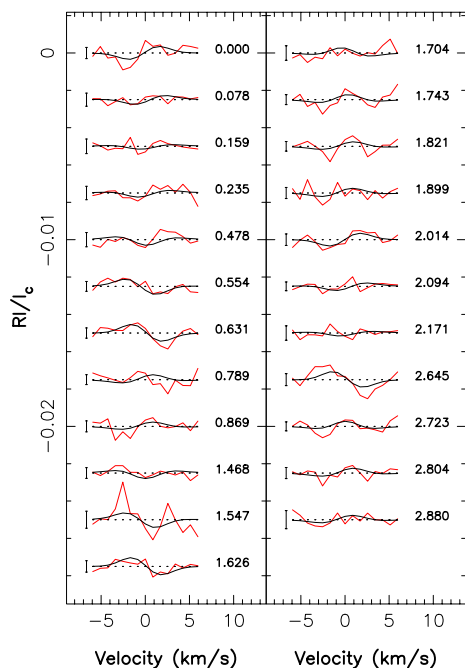


**Figure 9.** Temporal series of  $RI$  of GJ 358. Data are in red, the modeled  $RI$  are in black. On the right of each spectrum, we indicate the observation phase, on the left the  $1\text{-}\sigma$  error bars.

data (see Table 9) using the two different imaging methods (based on  $I$  and  $I'$ ) with that derived from the multiple sine fits of  $v_r$  (with fundamental + 1 to 3 harmonics), and from the usual anti-correlation observed between  $v_s$  and  $v_r$  (e.g., see Melo et al. 2007, for more details). From these results, we clearly see that the quality of the filtering based on Doppler imaging is similar to the one obtained from the multiple sine-fit (fundamental + two first harmonics), and much better than that based on the anti-correlation between  $v_s$  and  $v_r$ . More specifically and with respect to the latter case, we decrease the rms dispersion by a factor of 5 to 8 (depending on the  $v \sin i$ ).

The use of the profile residuals  $RI$  can lead to a small underestimate of the equivalent spot area epsilon (for smaller values of  $v \sin i$  in particular), however the RV filtering is not affected reaching down to almost the noise level with both methods.

Finally, the density of the sampling does not affect much the quality of the reconstructed RVs, as long as it is dense and even enough (typically a few tens of observing points covering a few rotation cycles). The lowest the  $v \sin i$ , the stronger the importance of the sampling.

### 5.3 Application to M dwarfs

We apply the residual imaging method presented and tested in Sec. 5.1 & 5.2 to recover the parent spot distribution generating the observed RV activity jitter for the various stars of our sample.

To assess the likelihood of the RV fit we obtain from the map, we compute the FAP as presented in Sec. 4.2.2. We take the multiple sine fit of  $v_r$  (fundamental + 2 first harmonics) as a reference to compute  $\Delta\chi^2$ ; we then obtain (with a formula resembling Eq.3) :

$$\Delta\chi^2 = \frac{\chi_{r,0}^2 - \chi_{r,2}^2}{\chi_{r,1}^2} \cdot N \quad (5)$$

with  $\chi_{r,1}^2$  and  $\chi_{r,2}^2$ , respectively, corresponding to the  $\chi_r^2$  of the multiple sine fit and of the fit obtained with the Doppler imaging based on residual reconstruction (hereafter DI fit). The number of degrees of freedom associated with the imaging process is estimated from the number of parameters associated with the non-axisymmetric SH modes needed to describe the observed variations, i.e.,  $\sim 20$  for  $l \leq 4$ . Results are presented in Table 6.

#### 5.3.1 GJ 358

From the  $RI$  profiles (see Fig. 9), we reconstruct the map shown in Fig. 10, featuring an equivalent spot coverage  $\epsilon$  of  $\sim 1\%$  (with  $b = 0.5$ ). The initial  $\chi_r^2$  is 3.8 and corresponds to the fit to the  $RI$  spectra with an unspotted star. Adding spots on the stellar surface allows the code to reduce  $\chi_r^2$  down to 2.1, with a main spot at high latitude ( $\sim 60^\circ$ ), and extending towards the equator.

Synthetic RV curve derived from this brightness map exhibits a full amplitude of  $8.5 \text{ m s}^{-1}$ , and matches the data down to  $\chi_{r,2}^2 = 2.05$ . The rms of the RV residuals is  $2.88 \text{ m s}^{-1}$  (whereas  $\sigma_0 = 2.08 \text{ m s}^{-1}$ ). The low FAP ( $< 0.01\%$ ) demonstrates that the imaging process provides a very significant improvement in the quality of the fit to the data. Moreover, in the  $v_r$  periodograms we clearly see that (i) the signals at  $P_{\text{rot}}$ ,  $P_{\text{rot}}/2$  and  $P_{\text{rot}}/3$  have been removed, and (ii) no major periodic signal remains.

#### 5.3.2 GJ 479

The reconstructed spots have a equivalent surface of  $\sim 1.4\%$ , and are located at mid-latitude ( $\sim 40^\circ$ , see Fig. H1). It corresponds to a final  $\chi_r^2$  of 2.9 (starting from  $\chi_r^2 = 5.0$ ).

The  $J_m$  component of the RV jitter deduced from this map has a peak-to-peak amplitude of  $11 \text{ m s}^{-1}$ , and the rms of RV residuals is  $3.93 \text{ m s}^{-1}$ . Once  $J_m$  is subtracted from RV data, the periodogram does not exhibit any strong peak anymore: the filtering allows to clean up the signals whose periods are  $P_{\text{rot}}$ ,  $P_{\text{rot}}/2$ ,  $P_{\text{rot}}/3$ .

#### 5.3.3 GJ 410

For GJ 410, we collected observations over three months (i.e., six stellar rotations). We note that all the  $RI$  spectra do not identically repeat from one rotation cycle to the next (see, e.g., phases 2.7 and 3.7, or phases 4.9 and 5.9 in Fig. 11). For this star, one of the most active of the studied sample, we first carried out a reconstruction for the whole data set (see Fig. H2). In a second step, we divided the data set into three sequential subsets to take into account the evolution of spot coverage on the stellar surface, respectively corresponding to rotation cycles 1.928-2.707 (epoch #1, 9 observations), 3.777-4.988 (epoch #2, 12 obs) and 5.058-6.199 (epoch #3, 7 obs). The results are given Fig. 12.

Dividing the data into multiple subsets allows us to improve the fit to the data, with a final  $\chi_r^2$  decreased from 2.0 (for the complete set) to 1.2-1.7 (for the individual subsets). The reconstructed maps show that in epoch #1 a main dark spot at low latitude around phase 0.6 is visible at the stellar surface, with a fainter spot at phase 0.25 and  $30^\circ$  of latitude. This secondary spot grows and strengthens in epoch #2 and #3, and a new spot appears at phase 0.95 from epoch #2 onwards.

Moreover, the quality of the RV filtering increases within

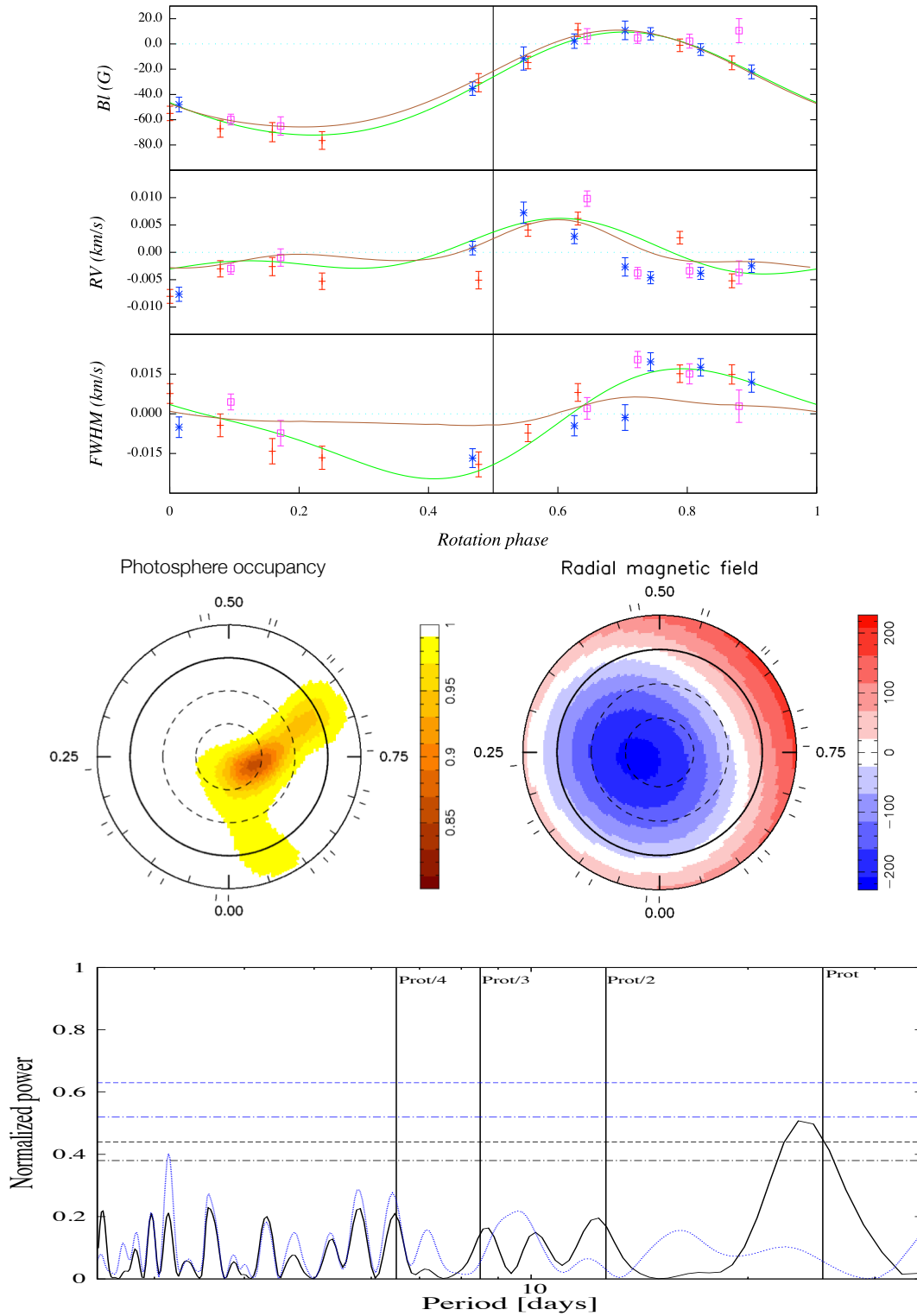


**Figure 10.** *Top:* Temporal evolution of  $B_l$ ,  $v_r$  and FWHM (with respect to the average value) of GJ 358. Data and their error bars are represented in red, blue and pink according the rotation cycle (cycle 1 in red, cycle 2 in blue and cycle 3 in pink). The green curves corresponds to the sine fit, and the brown curves represents the RVs computed from the DI map (white means that there is only quiet photosphere, brown means there is only spot in the cell), and *Middle left:* Maps of the filling factor of the photosphere, and *Middle right:* Map of the radial large-scale magnetic field. *Bottom:* Periodograms of observed RVs (black), and of the RVs after the RV filtering from DI (blue). The FAP at 1% and 10% are represented in dotted lines and dot-dashed lines.



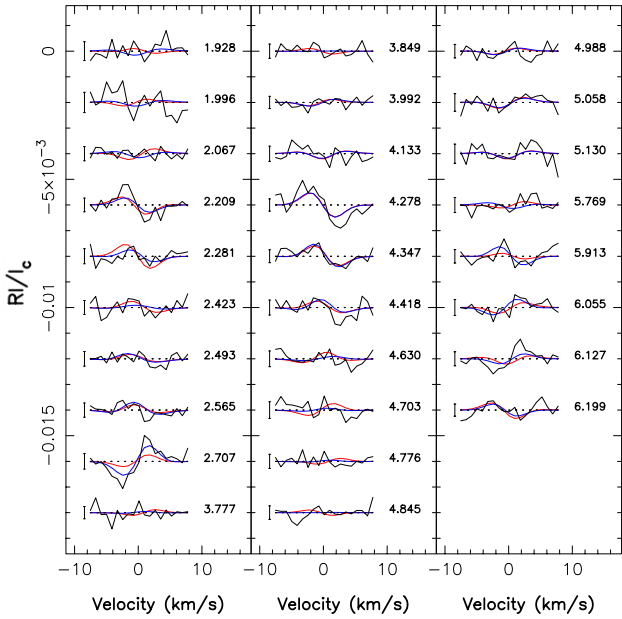


**Figure 11.** As Fig. 9, for GJ 410. The blue fit represents the fit from epochs #1 to #3, the red fit represents the fit from the full data set.

each of our subsets. The modeled RV curves we derive match the observed ones at a  $\chi_r^2$  level of 1.0-1.9, to be compared with 4.1 when processing the whole data set. We conclude that in the case of GJ 410, the main variability observed in RV data likely comes from short-lived spots, inducing an evolution in the shape of the RV curve on a timescale of only 2 rotation cycles.

### 5.3.4 GJ 205

For GJ 205, the amplitude of the  $RI$  spectra is low ( $\leq 0.05\%$ , see Fig. G1). The DI reconstruction leads to an equivalent spotted area  $\epsilon$  of  $\sim 0.9\%$  that allows to decrease the  $\chi_r^2$  fit to the profiles from 4.3 to 3.8 only. The reconstructed features exhibit faint spot clusters, located at high and mid-latitude, however, this reconstruction is not reliable given the FAP of 75% associated with the Stokes  $I$  LSD fit. The RV jitter is not efficiently filtered (FAP  $\sim 98\%$ ). These results validate that there is likely no signals at  $P_{\text{rot}}$  and that DR might strongly affect the dark spot location at the surface of GJ 205 and thus the RV activity jitter of the star. Further work, taking explicitly into account differential rotation, is thus needed for this star. This would require in particular a high quality spectropolarimetric data set from which differential rotation can be reliably estimated.

### 5.3.5 Discussion

The efficiency of the RV filtering depends on the relative importance of the rotationally modulated RV component with respect to the random component. The importance of each component is reminded in Table 11.

For the lowest mass star of this sample, GJ 358, the rotational modulated component  $J_m$  of the RV jitter have been divided by 2.8

(and  $J_{\text{tot}}$  by 2.2). For the earliest M-dwarfs (GJ 205 and GJ 410), neither the DI modeling nor the multiple sine fit succeed at obtaining a decent match to the observed RV jitter (high FAP), because of a higher level of intrinsic variability of the RV curve. In the particular case of GJ410, we observe that this higher level of intrinsic variability is directly related to the short spot lifetimes (1-2 rotation cycles), as evidenced by the significant improvement in the efficiency of the DI filtering when considering shorter time intervals (see Table 11). Contrary to a simple multiple sine fit, the use of the imaging techniques allows one to (i) to better constrain the origin of the activity jitter (dark spots and rotational modulation, DR or short spot lifetime), and (ii) to obtain a self-consistent physically-motivated, though still simple, description of the activity jitter rather than to perform a blind filtering of the RV data.

Our model is based on the assumption that the dominant contribution to the total RV signal in the M dwarfs should be the effect of dark spots. This assumption mainly relies on Sun-like stars studies, and on the low temperature of M dwarfs. However, we have to note that the current DI model does not yet allow us to faithfully reproduce the full amplitude of FWHM of the four studied stars. The phase of the variations are fitted, but the peak-to-peak amplitude is always underestimated in each case. This caveat may reflect inadequate assumptions/approximations in our modeling and will be further explored in forthcoming papers. The next step will be to add more physical realism in our model (*e.g.*, use a more realistic line profile  $I_s$  to characterize the spotted regions) to improve the modeling of the effects of the activity jitter in M dwarfs.

## 6 SUMMARY AND PERSPECTIVES

The magnetic analysis gives access to the large-scale magnetic field map of the observed weakly-active M dwarfs, as well as to a reliable and accurate estimate of  $P_{\text{rot}}$ . Fig. 13 summarizes the magnetic properties of our sample. These data allow us to add new observations in the  $M_\star - P_{\text{rot}}$  diagram, covering a mostly unexplored domain so far. The magnetic fields detected for the early-M dwarfs exhibit strengths of a few tens of G, and are lower by a factor 5 than those of more active and rapidly rotating mid-M dwarfs (Morin et al. 2008b). We note that for the stars with a stellar mass larger than  $0.5 M_\odot$ , the toroidal component is significant, except for GJ 205 whose large-scale magnetic field is dominated by a poloidal component. GJ 205 is the only observed star with a Rossby number  $R_o$  higher than 1 (as the Sun). This is in agreement with the trends previously reported in Donati & Landstreet (2009), where stars with  $R_o > 1$  tend to exhibit weak poloidal fields mostly aligned with the rotation axis.

For  $M_\star < 0.5 M_\odot$ , the large-scale magnetic properties are diverse, with some stars featuring mainly poloidal and axisymmetric fields (GJ 358, GJ 674) and some others exhibiting more complex topologies (GJ 479, GJ 176). In particular, we note that 2 stars of our sample feature different types of fields while sharing the same location in the  $M_\star$  vs  $P_{\text{rot}}$  plane. This is reminiscent of the bi-stable behavior of dynamo processes, as previously pointed out by, *e.g.*, Morin et al. (2011) in the case of active very low-mass dwarfs. The theoretical models (*e.g.*, Gastine et al. 2013) foresee a bistability around  $R_o = 0.1$ , with a transition between fields with a simple dipolar topology ( $R_o < 0.1$ ) and fields with a complex topology

<sup>6</sup>  $R_o$  is defined as  $R_o = P_{\text{rot}}/\tau_c$ , where  $\tau_c$  is the convective turnover time derived by Kiraga & Stepien (2007) from the rotation-activity relation in X-rays

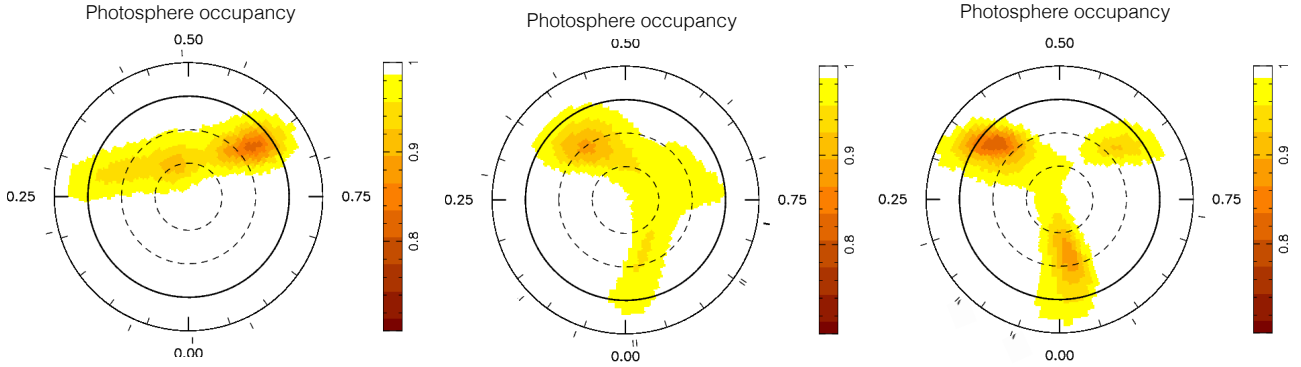


**Figure 12.** Maps of the filling factor of the photosphere of GJ 410 (white means that there is only quiet photosphere, brown means there is only spot in the cell) at the three epochs (from (1) to (3), from left to right).

	Raw RV data			Multiple sine-fit (fund. + 1 or 2 harm.)			DI modeling					
	$\sigma_0$ ( $\text{m s}^{-1}$ )	$\text{rms}_0$ ( $\text{m s}^{-1}$ )	$\chi^2_{r,0}$	$\text{rms}_1$ ( $\text{m s}^{-1}$ )	$\chi^2_{r,1}$	FAP (%)	RV curves			LSD profiles		
							$\text{rms}_2$ ( $\text{m s}^{-1}$ )	$\chi^2_{r,2}$	FAP (%)	$\chi^2_{r,i}$	$\chi^2_{r,f}$	FAP (%)
epoch #1	3.43	9.64	8.40	3.43	1.0	$\leq 0.01$	4.67	1.92	$\leq 0.01$	2.8	1.7	$\leq 0.01$
epoch #2	3.22	7.14	6.29	3.83	1.03	$\leq 0.01$	3.95	1.66	$\leq 0.01$	2.5	1.6	$\leq 0.01$
epoch #3	3.06	5.94	3.91	3.06	1.0	$\leq 0.01$	3.19	1.02	17	2.2	1.2	$\leq 0.01$
full set	3.28	8.84	7.85	6.55	3.96	0.04	6.78	4.14	2.8	2.9	2.0	$\leq 0.01$

**Table 10.** Same as Table 6 for the three observation epochs of GJ 410. For the observation epochs (1) and (3) a single harmonics is sufficient to reach residual RVs lower than  $3 \text{ m s}^{-1}$ . The RV jitter can be entirely modeled with rotational modulation ( $\text{rms}_{J,r} \sim 0 \text{ m s}^{-1}$ , et  $\text{rms}_{J,tot} \sim \text{rms}_{J,m}$ ), and we choose  $\chi^2_{r,1} = 1.0$  and  $\text{rms}_1 = \sigma_0$ .

	$J_{\text{tot}}$	$J_m$	$J_r$	$J_m$ with DI	$A_1$	$A_2$	$A_3$
	(m s <sup>-1</sup> )						
GJ 205	3.21	1.75	2.68	1.53	1.2	1.1	2.1
GJ 410	8.21	5.67	5.93	5.82	1.4	1.3	3.1
epoch #1	9.01	9.01	-	8.43	-	3.8	3.9
epoch #2	6.37	6.02	2.07	5.95	3.1	2.8	6.6
epoch #3	5.10	5.10	-	5.04	-	5.2	6.5
GJ 479	4.89	3.83	3.04	3.54	1.7	1.5	2.6
GJ 358	4.31	4.10	1.33	3.83	3.2	2.2	2.8

**Table 11.** Same as Table 7, with three additional columns: column 5 gives  $J_m$ , the rms of the RV data modelled using the DI imaging, column 7 gives  $A_2$ , quantifying how we can reduce the activity jitter thanks to DI imaging, and column 8 gives  $A_3 = J_m / \sqrt{J_m^2 - J_{m,DI}^2}$ , denoting the factor of decrease of the  $J_m$  component. The dash indicates that data can be reproduced down to the noise level, *i.e.*, that the RV variations are due to rotational modulations only.

( $R_o > 1$ ). Our observations suggest that dynamo bi-stability may indeed be present at different places of the  $M_\star$  vs  $P_{\text{rot}}$  diagram than previously identified by [Morin et al. \(2011\)](#) and whose relation with theoretical predictions is yet to be checked in more details. More spectropolarimetric observations of M dwarfs in this range of mass and rotation periods are necessary to investigate this result in more details.

To find an Earth-like planet (in terms of size, mass and ef-

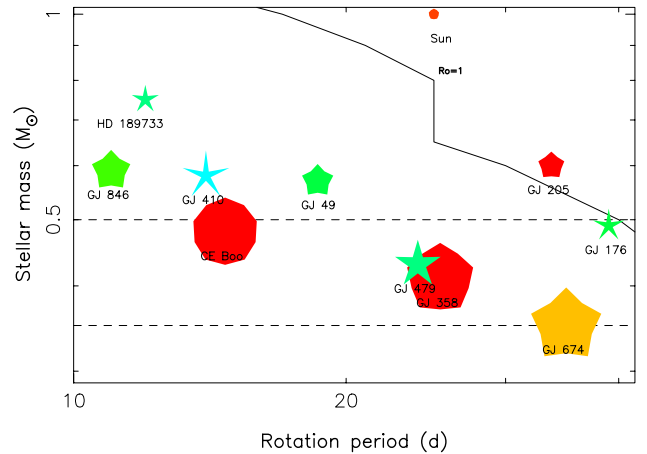


**Figure 13.** Properties of the magnetic topologies of our sample of five M dwarfs as a function of rotation period and stellar mass. Larger symbols indicate larger magnetic fields while symbol shapes depict the different degrees of axisymmetry of the reconstructed magnetic field (from decagons for purely axisymmetric fields to sharp stars for purely non-axisymmetric fields). Colors illustrate the field configuration (dark blue for purely toroidal fields, dark red for purely poloidal fields and intermediate colours for intermediate configurations). The solid line represents the contour of constant Rossby number  $R_o = 1$ . The dotted line correspond to the 0.5 and 0.35  $M_\odot$  thresholds. The Sun, GJ 49 and CE Boo ([Donati et al. 2008](#)), HD 189733 ([Fares et al. 2010](#)) and GJ 674 & GJ 176 presented in detail in a forthcoming paper are shown for comparison.

fective stellar flux) thanks to the RV method, moderately active M dwarfs appear to be natural targets with their reduced effective temperature and their low-mass. However we still need to model and filter out the RV activity jitter to reveal these plausible low-mass planets RV signatures. To characterize the activity jitter of cool low-mass stars, we used the studies done for Sun-like stars (*e.g.*, Dumusque et al. 2014), taking into account their reduced photospheric temperature. We then assumed the dominant contributor to the activity-modulated RV signal that plagues RV data is the rotational modulation caused by dark spot at the stellar surface (in agreement with theoretical studies as Beeck et al. 2015). With this hypothesis, we were able to develop a technique, based on a tomographic imaging (ZDI), to model the spot distribution at the surface of the four weakly active early M dwarfs we observed.

The sampled stars being slow rotators ( $v \sin i \leq 2 \text{ km s}^{-1}$ ), the observed spectral line width reflects directly intrinsic profiles rather than the Doppler broadening. To overcome this issue, we adapted the Doppler Imaging technique to reconstruct the profile residuals instead of the observed profiles themselves (see Sec. 5.1). Thanks to this approach, we are not dependent anymore on our ability at achieving a detailed description of the local profile, and the code is focussed on the profile distortion modeling only. Besides, this method relies on the knowledge of the rotational period  $P_{\text{rot}}$ , parameter previously estimated from the magnetic analysis.

The novel imaging method we devised is found to be reasonably successful at reconstructing the spot distribution at the surface of the early-type slowly-rotating stars that we studied. From this map and its associated set of spectra, we model the RV activity jitter whose period is commensurate to  $P_{\text{rot}}$ , *i.e.*,  $J_m$  component only. For our early M dwarf sample, we found that the spots cover up to 2% of the total stellar surface (in agreement with previous estimates for rapid rotators, see, *e.g.*, Morin et al. 2008a). The rotationally modulated RV component deduced from the brightness maps allows to reduce the observed RV jitter by a factor of 2-3, and the observed rotationally modulated component by a factor 3-6. The efficiency increases with decreasing stellar mass. For the earliest M dwarfs, we speculate that the high level of intrinsic variability likely caused by short-lived spots having lifetimes of  $< 2$  rotation cycles limits the efficiency of the modeling. A modeling of such effect is possible but requests specific observational strategy, with a high cadency sampling during more than 3 rotational cycles. Although relying on a simple assumption, this method gives promising results, and allows us to get a better insight on the origin of the activity RV jitter of early M dwarfs. This study of slowly-rotating early-M dwarfs complements the analysis already done for late M dwarfs (*e.g.*, Barnes et al. 2011, 2014, 2015).

To investigate if spot distributions relate to large-scale magnetic field topologies, we compare both the brightness and magnetic field maps that we obtained (see Fig. 14). It seems that the darkest spots concentrate either close to the magnetic poles (GJ 358 whose magnetic field is mainly poloidal), or to the magnetic equator (GJ 410 and GJ 479 whose magnetic field is significantly toroidal) - we exclude GJ 205 in this study, given the weak reliability of the spot distribution map. This suggests that the large-scale magnetic field may indeed be controlling where surface spots tend to preferentially appear at the stellar surface, as it does in the particular case of the Sun. This tendency needs to be examined in a larger sample with new spectropolarimetric surveys of moderately active M dwarfs. Besides, given that surface spot distributions are significantly impacting our ability at detecting Earth-like planets (see, *e.g.*, simulations done by Andersen & Korhonen 2015), it will be worthwhile to extent this study to later-type M dwarfs

to improve our knowledge of their spot patterns. For example, the Doppler Imaging is a powerful tool to investigate whether spot patterns change and, *e.g.*, evolve towards more even distributions of smaller features, when going from partially to fully convective stars.

Further improvements can to be implemented to obtain a more accurate filtering of the RV curves of M dwarfs (*e.g.*, by incorporating the temporal evolution of spots within the imaging process). Moreover, adapting our method to stars of other spectral types (G and K), for which the activity jitter is no longer dominated by the spot brightness contrast but by plages and the suppression of convective blueshift (*e.g.*, Haywood et al. 2014), is another obvious avenue worth exploring. Finally, a complementary study is in preparation to present the performances of this technique for M-dwarfs hosting a planet.

To disentangle stellar from planetary signals, a powerful analysis should be to carry out observations at both optical and IR wavelengths, particularly for M dwarfs emitting a large fraction of their flux in the IR. Several studies showed that the RV jitter will be divided by at least a factor of 2 due to the lower contrast between the dark spot regions and the quiet photosphere (Marchwinski et al. 2015) & Reiners et al. (2010); Rodler et al. (2011), respectively for Sun-like stars & late M dwarfs). In this context, the new generation of high resolution/precision velocimeters working in the nIR domain (*e.g.*, CARMENES<sup>7</sup>, SPIRou<sup>8</sup>, CRIRES+<sup>9</sup>) present a tremendous interest. However, characterizing, modeling and filtering out the RV activity jitter of M dwarfs remain mandatory steps for all future velocimetric studies aiming at detecting small Earth-mass rocky planets. They allow to define the best adapted observational strategies, taking into account the specificities of the M dwarf activity that hampers RV measurements. Moreover, while the brightness contrast decreases in the IR, the impact of small scale-magnetic field on RVs strengthens through Zeeman effect. Therefore, the method we presented will be particularly adapted for SPIRou, which will be both a high-precision velocimeter and a spectropolarimeter. Spectropolarimetric surveys in nIR will give new options for filtering RV curves from the activity jitter using tomographic techniques like ZDI, and will efficiently further enhance the sensitivity to low-mass planets, as well as to the magnetic stellar activity RV signal itself.

## ACKNOWLEDGEMENTS

This paper is based on observations obtained at the 3.6m telescope in La Silla, Chile, operated by ESO, the European Southern Observatory. We thank the La Silla staff for their valuable help throughout our observing runs and F.Bouchy for his help in the coordination of observing runs. We also thank the TBL staff for their help during data collection of GJ 410, GJ 205 and GJ 846. Finally we thank X.Bonfils for his M mask that we used to compute RVs. JM was sponsored by a postdoctoral fellowship of the Alexander von Humboldt foundation in Göttingen. The authors acknowl-

<sup>7</sup> Calar Alto high-Resolution search for M dwarfs with Exoearths with Near-infrared and optical Echelle Spectrographs, a high-precision velocimeter at the 3.5m telescope at the Calar Alto Observatory.

<sup>8</sup> SpectroPolarimeter in the near InfraRed, a spectropolarimeter/high-precision velocimeter for the 3.6m Canada-France-Hawaii Telescope. It will operate at near-infrared wavelengths (first light in 2017).

<sup>9</sup> upgrade of the CRyogenic InfraRed Echelle Spectrograph at ESO/VLT (first light in 2018).

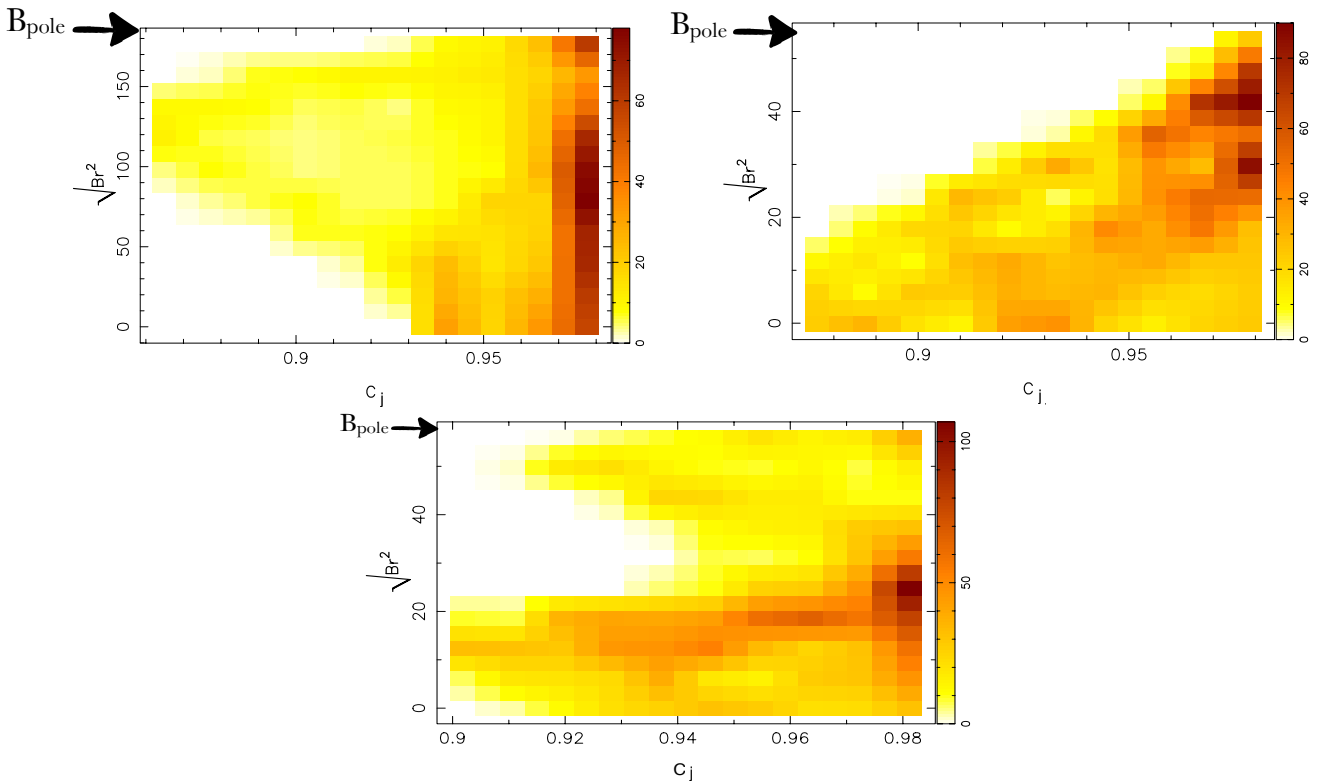


**Figure 14.** The x-axis depicts the  $C_j$ , denoting the proportion of photosphere inside each cell, and the y-axis the absolute value of the radial component of the large-scale magnetic field. The colorscale represents the number of cells affected by both a radial magnetic field and a dark spot. The arrow indicates the absolute value of the radial polar magnetic field of the star. *Top left* : GJ 358 *Top right* : GJ 479 *Bottom* : GJ 410.

edge the PNPS/INSU (Programme national de Physique Stellaire) to fund this project. XD acknowledges funding from the LabEx OSUG@2020. Finally thank you to the anonymous referee for the useful comments.

## REFERENCES

- Aigrain S., Pont F., Zucker S., 2012, *MNRAS*, 419
- Andersen J. M., Korhonen H., 2015, *MNRAS*, 448, 3053
- Baraffe I., Homeier D., Allard F., Chabrier G., 2015, *A&A*, 577, A42
- Barnes J., Jeffers S., Jones H., 2011, *MNRAS*, 412, 1599
- Barnes J. R., et al., 2014, *MNRAS*, 439, 3094
- Barnes J. R., Jeffers S. V., Jones H. R. A., Pavlenko Y. V., Jenkins J. S., Haswell C. A., Lohr M. E., 2015, *ApJ*, 812, 42
- Beeck B., Schüssler M., Cameron R. H., Reiners A., 2015, *A&A*, 581, A42
- Boisse I., et al., 2009, *A&A*, 495, 959
- Boisse I., Bouchy F., Hébrard G., Bonfils X., Santos N., Vauclair S., 2011, *A&A*, 528
- Bonfils X., et al., 2007, *A&A*, 474, 293
- Bonfils X., Gillon M., Udry S., Armstrong D., Bouchy F., 2012, *A&A*, 546, A27
- Bonfils X., Delfosse X., Udry S., Forveille T., Mayor M., Perrier C., Bouchy F., 2013, *A&A*, 549, A109
- Borgniet S., Meunier N., Lagrange A.-M., 2015, preprint, ([arXiv:1505.07361](https://arxiv.org/abs/1505.07361))
- Brown S. F., Donati J.-F., Rees D. E., Semel M., 1991, *A&A*, 250, 463
- Collier Cameron A., 1992, in Byrne P. B., Mullan D. J., eds, *Lecture Notes in Physics*, Berlin Springer Verlag Vol. 397, *Surface Inhomogeneities on Late-Type Stars*, p. 33, [doi:10.1007/3-540-55310-X\\_131](https://doi.org/10.1007/3-540-55310-X_131)
- Delfosse X., Forveille T., Ségransan D., Beuzit J.-L., Udry S., Perrier C., Mayor M., 2000, *A&A*, 364, 217
- Desort M., Lagrange A., Galland F., Udry S., Mayor M., 2007, *A&A*, 473, 983
- Donati J.-F., 2001, in Boffin H. M. J., Steeghs D., Cuypers J., eds, *Lecture Notes in Physics*, Berlin Springer Verlag Vol. 573, *Astromotography, Indirect Imaging Methods in Observational Astronomy*, p. 207
- Donati J.-F., 2003, p. 41
- Donati J., Landstreet J. D., 2009, *ARA&A*, 47, 333
- Donati J.-F., Semel M., Carter B. D., Rees D. E., Collier Cameron A., 1997, *MNRAS*, 291, 658
- Donati J.-F., Collier Cameron A., Petit P., 2003, *MNRAS*, 345, 1187
- Donati J.-F., Forveille T., Cameron A. C., Barnes J. R., Delfosse X., Jardine M. M., Valenti J. A., 2006a, *Science*, 311, 633
- Donati J.-F., et al., 2006b, *MNRAS*, 370, 629
- Donati J.-F., et al., 2008, *MNRAS*, 390, 545
- Dressing C. D., Charbonneau D., 2015, *ApJ*, 807, 45
- Dumusque X., Boisse I., Santos N., 2014, *ApJ*, 796
- Fares R., et al., 2010, *MNRAS*, 406, 409
- Forveille T., et al., 2009, *A&A*, 493, 645
- Gastine T., Morin J., Duarte L., Reiners A., Christensen U. R., Wicht J., 2013, *A&A*, 549, L5
- Gomes Da Silva J., Santos N., Bonfils X., Delfosse X., 2011, *A&A*, 534, A30
- Gray D. F., 1982, *ApJ*, 255, 200
- Haywood R., Collier-Cameron A., Quloz D., 2014, *MNRAS*, 443
- Hébrard E., Donati J., Delfosse X., Morin J., Boisse I., 2014, *MNRAS*, 443, 2899
- Kasting J. F., Kopparapu R., Ramirez R. M., Harman C. E., 2014, *Proceedings of the National Academy of Science*, 111, 12641
- Kiraga M., Stepien K., 2007, *Acta Astronomica*, 57, 149
- Koen C., Kilkeny F., van Wyk F., Marang F., 2010, *MNRAS*, 403, 1949
- Kurucz R., 1993, CDROM # 13 (ATLAS9 atmospheric models) and # 18 (ATLAS9 and SYNTHE routines, spectral line database). Smithsonian

Star	$p_{\text{rot}}^{B_l}$ (d)	$p_{\text{rot}}^{\text{RV}}$ (d)	$p_{\text{rot}}^{\text{FWHM}}$ (d)	$p_{\text{rot}}^{\text{H}\alpha}$ (d)
GJ 205	33.63±0.37	39.70±0.85	41.9±1.9	33.46±0.80
GJ 410	13.83±0.10	14.20±0.10	14.76±0.20	15.15±0.30
GJ 479	24.04±0.75	23.2±1.9	25.48±0.81	22.94±0.60
GJ 358	25.37±0.32	24.47±0.60	25.49±0.42	23.8±2.7

**Table A1.** Rotation periods derived from  $B_l$ , RV, FWHM and  $\text{H}\alpha$  measurements and the estimated error-bars at  $1\sigma$  for the 4 stars of the sample.

Astrophysical Observatory, Washington D.C.  
 Leggett S., Allard F., Geballe T., Hauschild P., Schweitzer A., 2001, *ApJ*, 548, 908  
 Lomb N. R., 1976, *Ap&SS*, 39, 447  
 Marchwinski R. C., Mahadevan S., Robertson P., Ramsey L., Harder J., 2015, *ApJ*, 798, 63  
 Mayor M., et al., 2003, *The Messenger*, 114, 20  
 Melo C., et al., 2007, *A&A*, 467, 721  
 Meunier N., Desort M., Lagrange A.-M., 2010, *A&A*, 512, A39  
 Morin J., et al., 2008a, *MNRAS*, 384, 77  
 Morin J., et al., 2008b, *MNRAS*, 390, 567  
 Morin J., Donati J., Petit P., Delfosse X., Forveille T., Jardine M. M., 2010, *MNRAS*, 407, 2269  
 Morin J., Dormy E., Schrunner M., Donati J.-F., 2011, *MNRAS*, 418, L133  
 Moutou C., et al., 2007, *A&A*, 473, 651  
 Queloz D., Henry G., Sivan J., Baliunas S., Beuzit J., Donahue R., 2001, *A&A*, 379  
 Reiners A., Bean J., Hubert K., Dreizler S., Seifahrt A., 2010, *ApJ*, 710, 432  
 Robertson P., Mahadevan S., Endl M., Roy A., 2014, *Science*, 345, 440  
 Rodler F., Del Burgo C., Witte S., Helling C., Hauschildt P. H., Martín E. L., Álvarez C., Deshpande R., 2011, *A&A*, 532, A31  
 Scargle J. D., 1982, *ApJ*, 263, 835  
 Snik F., Kochukhov O., Piskunov N., 2011, *ASP Conference Series*, 437, 237  
 Zechmeister M., Kürster M., 2009, *A&A*, 496, 577

## APPENDIX A: ROTATION PERIODS DERIVED FROM $B_l$ , RV, FWHM AND $\text{H}\alpha$ .

## APPENDIX B: OBSERVATIONS JOURNAL

Observations journal for the four M-dwarfs observed from October 2013 to August 2014 with HARPS-Pol@LaSilla and NARVAL@TBL.

## APPENDIX C: SUPPLEMENTARY $B_l$ DATA

## APPENDIX D: SUPPLEMENTARY STOKES V LSD PROFILES AND PARENT LARGE-SCALE MAGNETIC FIELD MAPS

## APPENDIX E: SUPPLEMENTARY $B_l$ , $v_r$ , FWHM, $\text{H}\alpha$ AND $v_s$ DATA

## APPENDIX F: COMPLEMENTARY RESULTS OF THE SIMULATIONS PRESENTED SEC. 5.2.

## APPENDIX G: SUPPLEMENTARY $RI$ SPECTRA

## APPENDIX H: SUPPLEMENTARY $B_l$ , $v_r$ AND FWHM RECONSTRUCTION, AND RELATIVE BRIGHTNESS MAPS

This paper has been typeset from a  $\text{\TeX}/\text{\LaTeX}$  file prepared by the author.

Cycle	Date	BJD (+ 2 456 000)	instrument	S/N	B (G)	RV (km s <sup>-1</sup> )
0.024	30apr14	778.5870	HARPS-Pol	133	20.54 ± 7.03	8.17e-03 ± 1.56e-03
0.069	01may14	779.6500	HARPS-Pol	121	3.36 ± 7.82	4.08e-03 ± 1.74e-03
0.151	03may14	781.6390	HARPS-Pol	108	8.61 ± 9.02	5.16e-03 ± 1.97e-03
0.190	04may14	782.5590	HARPS-Pol	135	5.46 ± 7.04	5.53e-03 ± 1.43e-03
0.231	05may14	783.5600	HARPS-Pol	102	24.94 ± 9.97	-6.72e-03 ± 2.09e-03
0.272	06may14	784.5480	HARPS-Pol	120	18.45 ± 8.25	5.52e-03 ± 1.75e-03
0.356	08may14	786.5590	HARPS-Pol	146	21.14 ± 6.50	1.32e-02 ± 1.43e-03
1.314	31may14	809.5840	HARPS-Pol	99	32.36 ± 9.77	7.16e-04 ± 2.20e-03
1.397	02jun14	811.5850	HARPS-Pol	120	16.67 ± 7.65	9.20e-04 ± 1.69e-03
1.523	05jun14	814.6220	HARPS-Pol	99	-16.66 ± 9.66	-4.61e-03 ± 2.14e-03
1.607	07jun14	816.6220	HARPS-Pol	95	-34.92 ± 10.45	-4.82e-03 ± 2.25e-03
1.648	08jun14	817.6150	HARPS-Pol	85	-16.75 ± 11.69	-4.24e-03 ± 2.31e-03
1.689	09jun14	818.6140	HARPS-Pol	75	-16.33 ± 13.67	-1.93e-03 ± 2.87e-03
1.729	10jun14	819.5700	HARPS-Pol	97	-24.67 ± 10.03	-5.63e-03 ± 2.18e-03
1.894	14jun14	823.5230	HARPS-Pol	89	1.53 ± 11.60	3.14e-03 ± 2.39e-03
1.935	15jun14	824.5230	HARPS-Pol	106	15.89 ± 9.20	5.63e-03 ± 1.96e-03
2.016	17jun14	826.4650	HARPS-Pol	113	14.38 ± 8.71	2.82e-03 ± 1.83e-03
2.099	19jun14	828.4620	HARPS-Pol	129	22.29 ± 7.44	2.27e-03 ± 1.60e-03
2.144	20jun14	829.5330	HARPS-Pol	118	10.17 ± 7.95	6.55e-03 ± 1.76e-03
2.184	21jun14	830.5110	HARPS-Pol	114	19.65 ± 8.41	4.76e-03 ± 1.82e-03
2.352	25jun14	834.5360	HARPS-Pol	101	40.06 ± 9.60	3.41e-03 ± 2.12e-03
2.643	02jul14	841.5440	HARPS-Pol	63	3.14 ± 17.37	2.85e-03 ± 3.50e-03
2.684	03jul14	842.5310	HARPS-Pol	101	-18.62 ± 9.72	-5.48e-03 ± 2.08e-03

**Table B1.** Journal of observations for GJ 479. Columns 1 and 5, respectively, list, the rotational cycle (computed with the rotation period mentioned in Table 1 according to ephemeris given by Eq 1, the date of the beginning of the night, the Barycentric Julian Date, the observation site, the peak S/N (per 0.85 km s<sup>-1</sup> velocity bin). Column 6-7 give, respectively,  $B_l$  and RV values.

Cycle	Date	BJD (+ 2 456 000)	instrument	S/N	B (G)	RV (km s <sup>-1</sup> )
0.000	17jan14	675.7090	HARPS-Pol	109	-51.09 ± 12.08	-6.39e-03 ± 1.93e-03
0.078	19jan14	677.6780	HARPS-Pol	96	-54.90 ± 14.22	-1.23e-03 ± 2.21e-03
0.158	21jan14	679.7130	HARPS-Pol	86	-99.91 ± 16.07	-8.14e-04 ± 2.47e-03
0.235	23jan14	681.6580	HARPS-Pol	93	-94.82 ± 14.74	-3.57e-03 ± 2.26e-03
0.477	29jan14	687.7800	HARPS-Pol	88	-49.06 ± 15.49	-3.10e-03 ± 2.43e-03
0.553	31jan14	689.7110	HARPS-Pol	123	-15.37 ± 10.66	5.98e-03 ± 1.68e-03
0.631	02feb14	691.6650	HARPS-Pol	121	-1.68 ± 10.99	8.18e-03 ± 1.73e-03
0.789	06feb14	695.6510	HARPS-Pol	123	18.37 ± 10.49	4.64e-03 ± 1.71e-03
0.869	08feb14	697.6850	HARPS-Pol	113	10.17 ± 11.80	-3.22e-03 ± 1.88e-03
1.468	23feb14	712.8430	HARPS-Pol	112	-53.01 ± 11.43	2.75e-03 ± 1.85e-03
1.547	25feb14	714.8380	HARPS-Pol	76	-13.01 ± 18.93	9.27e-03 ± 2.86e-03
1.626	27feb14	716.8240	HARPS-Pol	107	-8.13 ± 12.01	4.92e-03 ± 1.99e-03
1.704	01mar14	718.8090	HARPS-Pol	86	7.23 ± 15.59	-7.48e-04 ± 2.51e-03
1.743	02mar14	719.8050	HARPS-Pol	119	12.56 ± 10.58	-2.58e-03 ± 1.78e-03
1.821	04mar14	721.7630	HARPS-Pol	124	-9.67 ± 9.97	-1.89e-03 ± 1.70e-03
1.899	06mar14	723.7550	HARPS-Pol	109	-29.50 ± 11.70	-4.77e-04 ± 1.96e-03
2.014	09mar14	726.6640	HARPS-Pol	106	-49.88 ± 12.37	-5.61e-03 ± 2.02e-03
2.094	11mar14	728.6900	HARPS-Pol	133	-81.82 ± 9.12	-9.77e-04 ± 1.56e-03
2.171	13mar14	730.6400	HARPS-Pol	86	-83.74 ± 15.55	1.07e-03 ± 2.49e-03
2.645	25mar14	742.6240	HARPS-Pol	101	-22.29 ± 12.71	1.19e-02 ± 2.12e-03
2.723	27mar14	744.5980	HARPS-Pol	130	12.28 ± 9.45	-1.70e-03 ± 1.60e-03
2.804	29mar14	746.6290	HARPS-Pol	107	7.83 ± 11.74	-1.37e-03 ± 1.97e-03
2.880	31mar14	748.5630	HARPS-Pol	70	16.42 ± 19.71	-1.72e-03 ± 3.16e-03

**Table B2.** Same as Table B1 for GJ 358.

Cycle	Date	BJD (+ 2 456 000)	instrument	S/N	B (G)	RV (km s <sup>-1</sup> )
0.000	03oct13	569.8850	HARPS-Pol	177	8.29 ± 2.25	-1.05e-05 ± 1.23e-03
0.030	04oct13	570.9030	HARPS-Pol	196	11.79 ± 2.00	-4.79e-03 ± 1.12e-03
0.178	09oct13	575.8680	HARPS-Pol	228	3.30 ± 1.70	-6.62e-04 ± 8.86e-04
0.208	10oct13	576.8910	HARPS-Pol	219	5.16 ± 1.80	9.26e-04 ± 9.94e-04
0.444	18oct13	584.8280	HARPS-Pol	188	11.05 ± 2.13	1.51e-03 ± 1.17e-03
0.505	20oct13	586.8820	HARPS-Pol	194	4.40 ± 2.04	2.49e-03 ± 1.14e-03
0.682	26oct13	592.8720	HARPS-Pol	210	-5.45 ± 1.84	-7.92e-04 ± 1.04e-03
0.741	28oct13	594.8510	HARPS-Pol	171	-2.36 ± 2.33	7.87e-04 ± 1.28e-03
0.918	03nov13	600.8070	HARPS-Pol	180	6.55 ± 2.20	6.62e-03 ± 1.22e-03
0.977	05nov13	602.8160	HARPS-Pol	189	11.98 ± 2.09	1.44e-03 ± 1.07e-03
1.036	07nov13	604.7880	HARPS-Pol	197	11.14 ± 2.00	3.71e-03 ± 1.12e-03
1.274	15nov13	612.7990	HARPS-Pol	170	2.45 ± 2.36	1.69e-03 ± 1.30e-03
1.332	17nov13	614.7790	HARPS-Pol	203	8.53 ± 1.94	-1.66e-03 ± 1.09e-03
1.571	25nov13	622.8050	HARPS-Pol	209	2.80 ± 1.88	-4.04e-03 ± 9.73e-04
1.623	27nov13	624.5610	NARVAL	313	-1.60 ± 1.31	-
1.630	27nov13	624.8090	HARPS-Pol	174	-2.16 ± 2.32	2.68e-03 ± 1.15e-03
1.688	29nov13	626.7720	HARPS-Pol	185	-4.40 ± 2.13	-1.92e-03 ± 1.18e-03
1.745	01dec13	628.7000	HARPS-Pol	138	-5.52 ± 3.04	2.07e-04 ± 1.57e-03
1.864	05dec13	632.6810	HARPS-Pol	171	5.87 ± 2.39	1.84e-03 ± 1.26e-03
2.006	10dec13	637.4830	NARVAL	399	8.10 ± 0.97	-
2.065	12dec13	639.4620	NARVAL	454	6.75 ± 0.83	-
2.186	16dec13	643.5400	NARVAL	308	4.78 ± 1.31	-
3.135	17jan14	675.5440	HARPS-Pol	172	4.19 ± 2.42	3.61e-03 ± 1.26e-03
3.197	19jan14	677.6080	HARPS-Pol	148	3.78 ± 2.76	7.27e-03 ± 1.59e-03
3.315	23jan14	681.5910	HARPS-Pol	133	8.39 ± 3.11	8.42e-03 ± 1.52e-03
3.523	30jan14	688.5870	HARPS-Pol	171	5.48 ± 2.37	-4.19e-03 ± 1.27e-03

Table B3. Same as Table B1 for GJ 205.

Cycle	Date	BJD (+ 2 456 000)	instrument	S/N	B (G)	RV (km s <sup>-1</sup> )
0.000	10sep13	546.4638	NARVAL	301	2.71 ± 1.43	-
0.637	17sep13	553.4688	NARVAL	251	2.14 ± 1.80	-
1.092	22sep13	558.4694	NARVAL	282	-1.07 ± 1.57	-
1.269	24sep13	560.4200	NARVAL	318	-1.60 ± 1.36	-
2.629	09oct13	575.3856	NARVAL	278	3.12 ± 1.57	-
2.821	11oct13	577.4947	NARVAL	242	1.67 ± 1.82	-
2.902	12oct13	578.3830	NARVAL	297	1.19 ± 1.41	-
2.993	13oct13	579.3876	NARVAL	274	-2.93 ± 1.55	-
3.442	18oct13	584.3262	NARVAL	209	4.21 ± 2.21	-
4.622	31oct13	597.3060	NARVAL	189	2.37 ± 2.44	-
7.075	27nov13	624.2851	NARVAL	194	-6.40 ± 2.41	-
8.252	10dec13	637.2351	NARVAL	280	1.27 ± 1.57	-
8.434	12dec13	639.2356	NARVAL	305	1.98 ± 1.42	-
8.615	14dec13	641.2330	NARVAL	234	7.99 ± 1.92	-
8.709	15dec13	642.2580	NARVAL	291	4.24 ± 1.52	-
25.764	20jun14	829.8720	HARPS-Pol	91	17.14 ± 5.05	8.63e-03 ± 3.26e-03
25.950	22jun14	831.9170	HARPS-Pol	158	7.85 ± 2.62	1.08e-03 ± 1.78e-03
26.132	24jun14	833.9110	HARPS-Pol	140	8.96 ± 3.02	-9.73e-05 ± 2.15e-03
26.314	26jun14	835.9120	HARPS-Pol	100	2.19 ± 4.55	2.84e-03 ± 3.03e-03
28.311	18jul14	857.8880	HARPS-Pol	111	6.47 ± 4.01	1.08e-02 ± 2.93e-03
28.398	19jul14	858.8430	HARPS-Pol	141	-0.08 ± 2.96	8.27e-03 ± 2.00e-03
28.493	20jul14	859.8910	HARPS-Pol	129	2.69 ± 3.34	5.13e-03 ± 2.15e-03
28.761	23jul14	862.8310	HARPS-Pol	107	6.86 ± 7.38	8.41e-03 ± 2.78e-03
28.850	24jul14	863.8130	HARPS-Pol	119	10.93 ± 3.61	1.04e-02 ± 2.31e-03
28.940	25jul14	864.8020	HARPS-Pol	131	4.41 ± 3.28	9.71e-03 ± 1.98e-03
31.849	27aug14	896.8010	HARPS-Pol	102	-0.01 ± 4.45	5.91e-03 ± 2.70e-03

Table B4. Same as Table B1 for GJ 846.

Cycle	Date	BJD (+ 2 456 000)	instrument	S/N	B (G)	RV (km s <sup>-1</sup> )
0.558	09jan14	667.6948	NARVAL	282	-8.94 ± 1.50	-
0.696	11jan14	669.6198	NARVAL	255	5.28 ± 1.69	-
1.000	15jan14	673.8840	HARPS-Pol	90	16.52 ± 5.62	-1.97e-02 ± 3.85e-03
1.928	28jan14	686.8660	HARPS-Pol	84	27.53 ± 6.11	-2.79e-03 ± 4.41e-03
1.996	29jan14	687.8170	HARPS-Pol	79	8.28 ± 6.59	4.17e-03 ± 4.34e-03
2.067	30jan14	688.8200	HARPS-Pol	108	4.11 ± 4.55	-5.30e-04 ± 2.90e-03
2.209	01feb14	690.8100	HARPS-Pol	112	3.32 ± 4.35	1.31e-02 ± 3.06e-03
2.281	02feb14	691.8190	HARPS-Pol	103	-1.09 ± 4.75	9.54e-04 ± 3.32e-03
2.423	04feb14	693.7960	HARPS-Pol	110	-15.13 ± 4.41	2.79e-03 ± 3.08e-03
2.493	05feb14	694.7790	HARPS-Pol	106	-13.66 ± 4.66	3.50e-03 ± 3.23e-03
2.565	06feb14	695.7870	HARPS-Pol	109	-8.80 ± 4.45	6.28e-03 ± 3.13e-03
2.707	08feb14	697.7710	HARPS-Pol	100	10.94 ± 4.92	-2.21e-02 ± 3.40e-03
3.777	23feb14	712.7580	HARPS-Pol	123	34.21 ± 3.85	-2.86e-03 ± 2.59e-03
3.849	24feb14	713.7600	HARPS-Pol	107	30.37 ± 4.53	2.02e-03 ± 2.94e-03
3.992	26feb14	715.7630	HARPS-Pol	122	19.46 ± 3.86	-3.82e-03 ± 2.82e-03
4.133	28feb14	717.7440	HARPS-Pol	101	3.45 ± 4.82	4.44e-03 ± 3.37e-03
4.278	02mar14	719.7690	HARPS-Pol	125	-2.65 ± 3.82	2.06e-02 ± 2.52e-03
4.347	03mar14	720.7430	HARPS-Pol	118	-7.61 ± 4.02	8.56e-03 ± 2.69e-03
4.418	04mar14	721.7260	HARPS-Pol	103	-1.61 ± 4.73	8.66e-03 ± 3.61e-03
4.630	07mar14	724.7060	HARPS-Pol	98	9.48 ± 5.00	1.01e-03 ± 3.52e-03
4.703	08mar14	725.7160	HARPS-Pol	94	24.12 ± 5.32	2.93e-03 ± 3.62e-03
4.776	09mar14	726.7450	HARPS-Pol	108	16.25 ± 4.47	2.14e-03 ± 3.17e-03
4.845	10mar14	727.7130	HARPS-Pol	113	22.17 ± 4.30	-2.84e-03 ± 3.05e-03
4.988	12mar14	729.7070	HARPS-Pol	112	9.37 ± 4.23	-1.80e-04 ± 2.84e-03
5.058	13mar14	730.6860	HARPS-Pol	89	6.96 ± 5.69	-6.63e-03 ± 3.84e-03
5.130	14mar14	731.6960	HARPS-Pol	83	7.69 ± 6.25	-5.06e-03 ± 4.48e-03
5.769	23mar14	740.6520	HARPS-Pol	103	16.34 ± 4.84	-5.91e-03 ± 3.06e-03
5.913	25mar14	742.6630	HARPS-Pol	113	11.95 ± 4.27	2.96e-03 ± 2.85e-03
6.036	27mar14	744.3780	NARVAL	169	11.67 ± 2.85	-
6.055	27mar14	744.6480	HARPS-Pol	97	5.46 ± 5.06	-8.96e-03 ± 3.52e-03
6.127	28mar14	745.6580	HARPS-Pol	110	6.51 ± 4.45	-1.39e-02 ± 3.09e-03
6.199	29mar14	746.6660	HARPS-Pol	124	-3.10 ± 3.82	1.81e-03 ± 2.76e-03
6.753	06apr14	754.4280	NARVAL	221	11.83 ± 2.09	-
6.899	08apr14	756.4720	NARVAL	298	11.17 ± 1.43	-
6.969	09apr14	757.4440	NARVAL	303	7.82 ± 1.42	-
7.119	11apr14	759.5440	NARVAL	262	4.32 ± 1.73	-
7.184	12apr14	760.4620	NARVAL	281	1.66 ± 1.53	-
7.255	13apr14	761.4560	NARVAL	296	-0.22 ± 1.47	-
7.323	14apr14	762.4040	NARVAL	229	-2.88 ± 1.91	-
7.399	15apr14	763.4680	NARVAL	294	-6.74 ± 1.47	-
7.468	16apr14	764.4370	NARVAL	300	-7.45 ± 1.45	-
7.542	17apr14	765.4620	NARVAL	253	-4.75 ± 1.76	-

**Table B5.** Same as Table B1 for GJ 410.



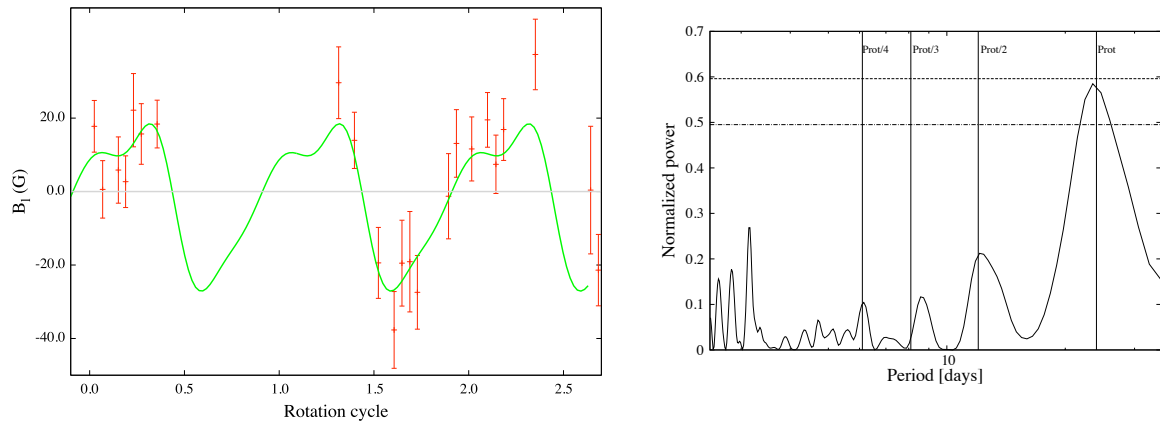


Figure C1. Same as Fig. 1 for GJ 479.

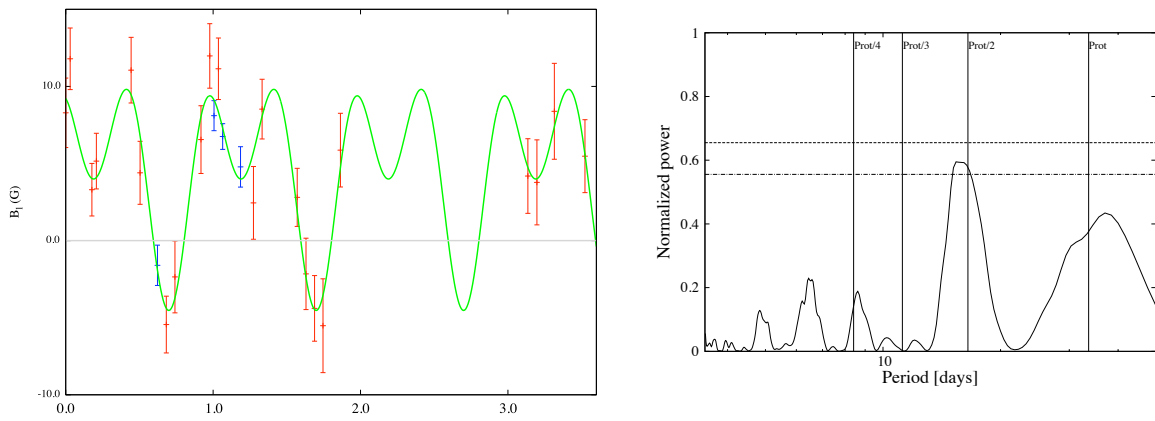
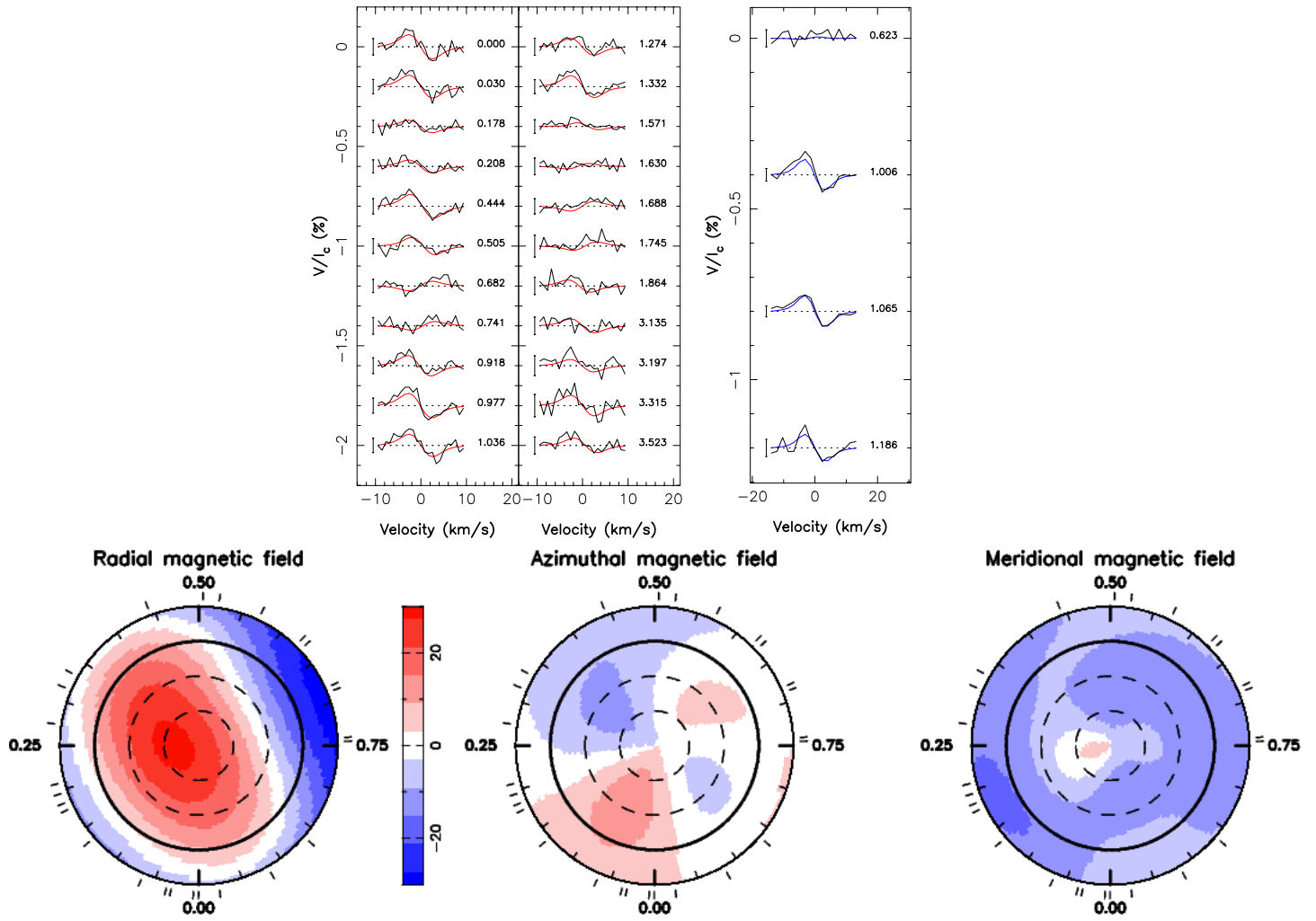


Figure C2. Same as Fig. 1 for GJ 205. HARPS-Pol data are in red, NARVAL data are blue.



**Figure D1.** Same as Fig. 3 for GJ 205. LSD Stokes V profiles in the top left and top right panels correspond to HARPS-Pol and NARVAL observations respectively.

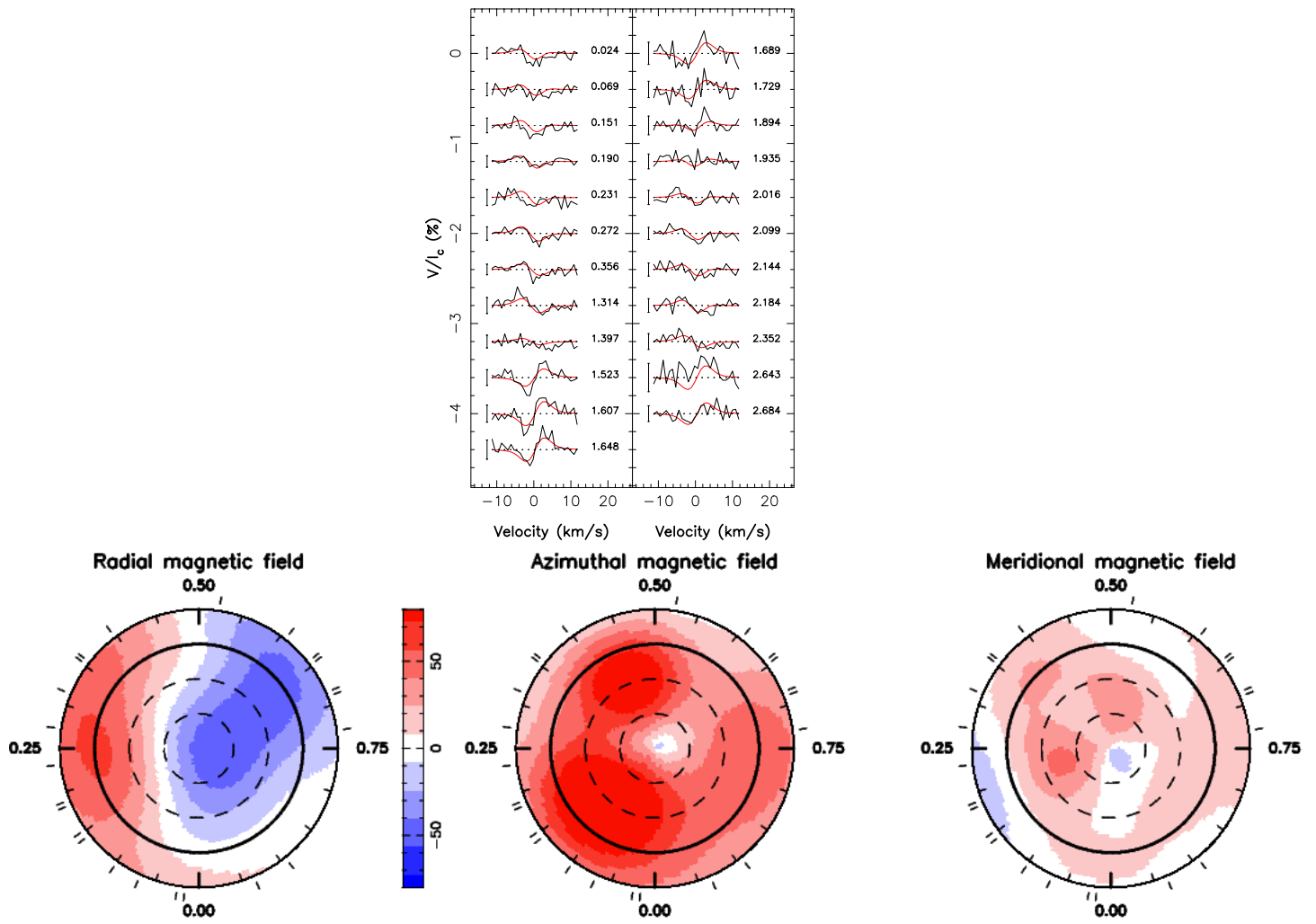
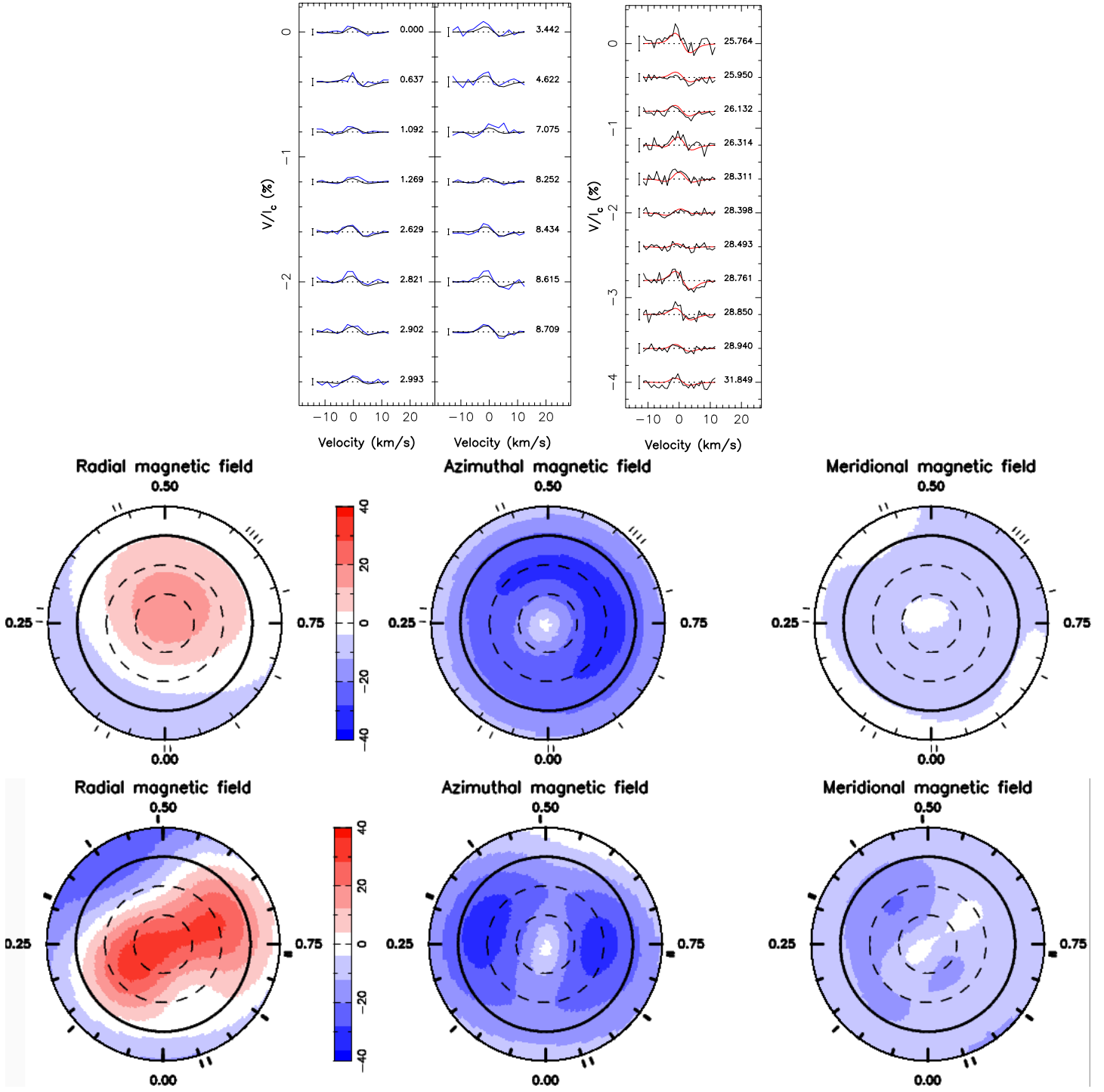


Figure D2. Same as Fig. 3 for GJ 479.



**Figure D3.** Same as Fig. 3 for GJ 846. LSD Stokes V profiles in the top left and top right panels correspond to NARVAL and HARPS-Pol observations respectively.

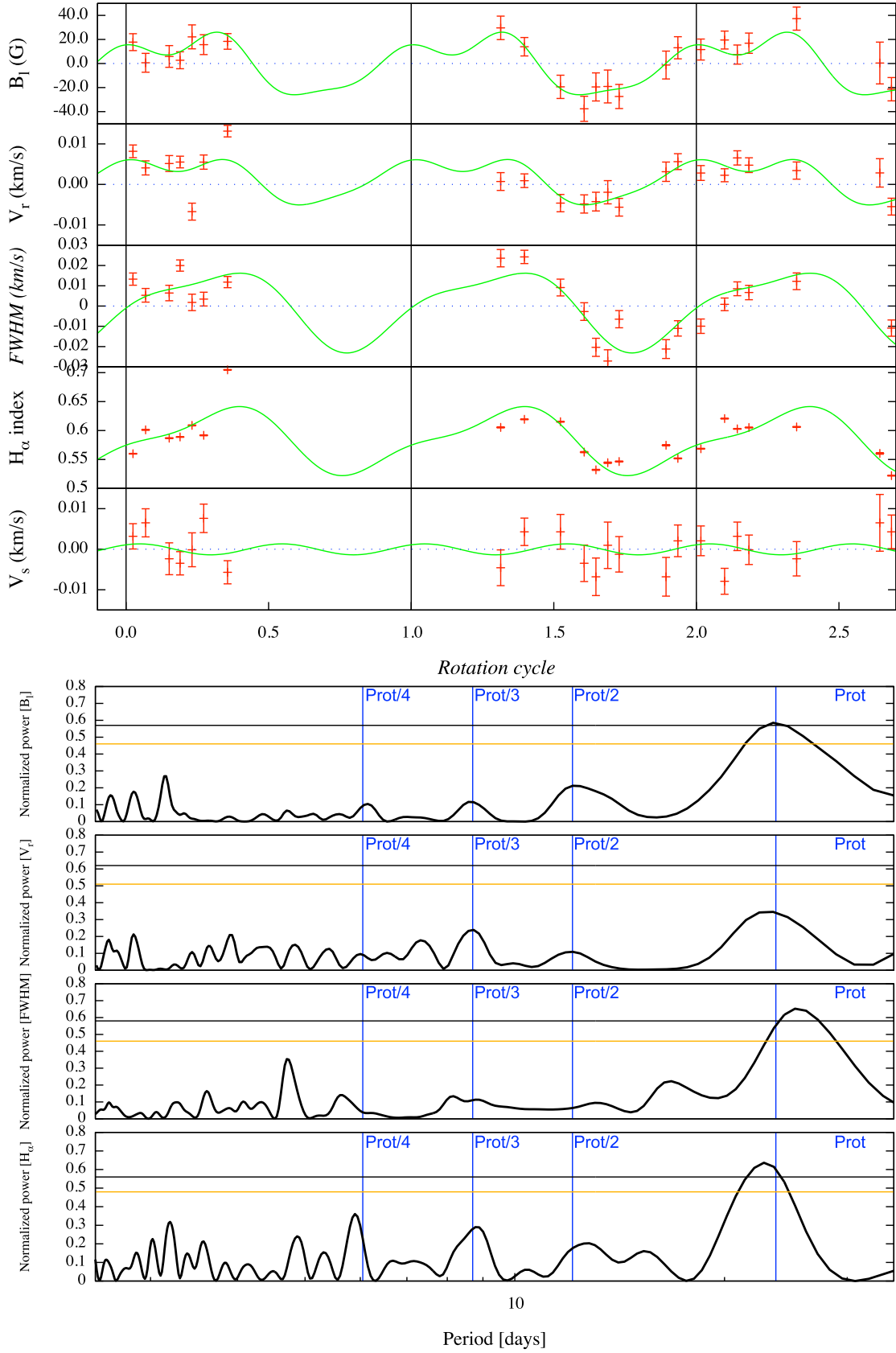
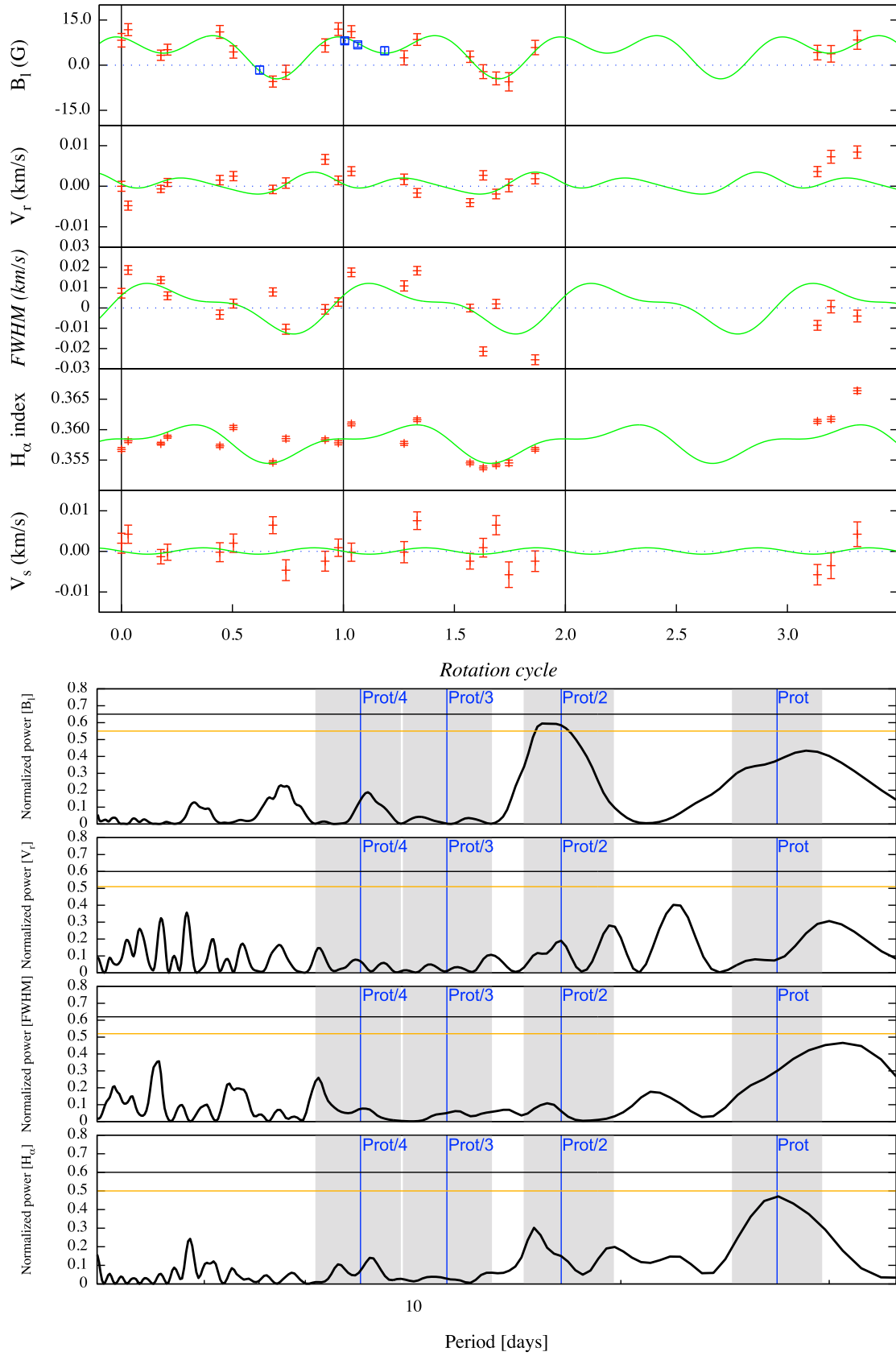
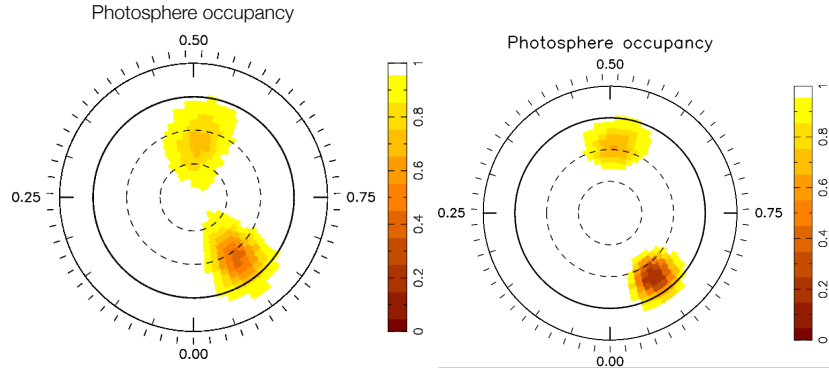


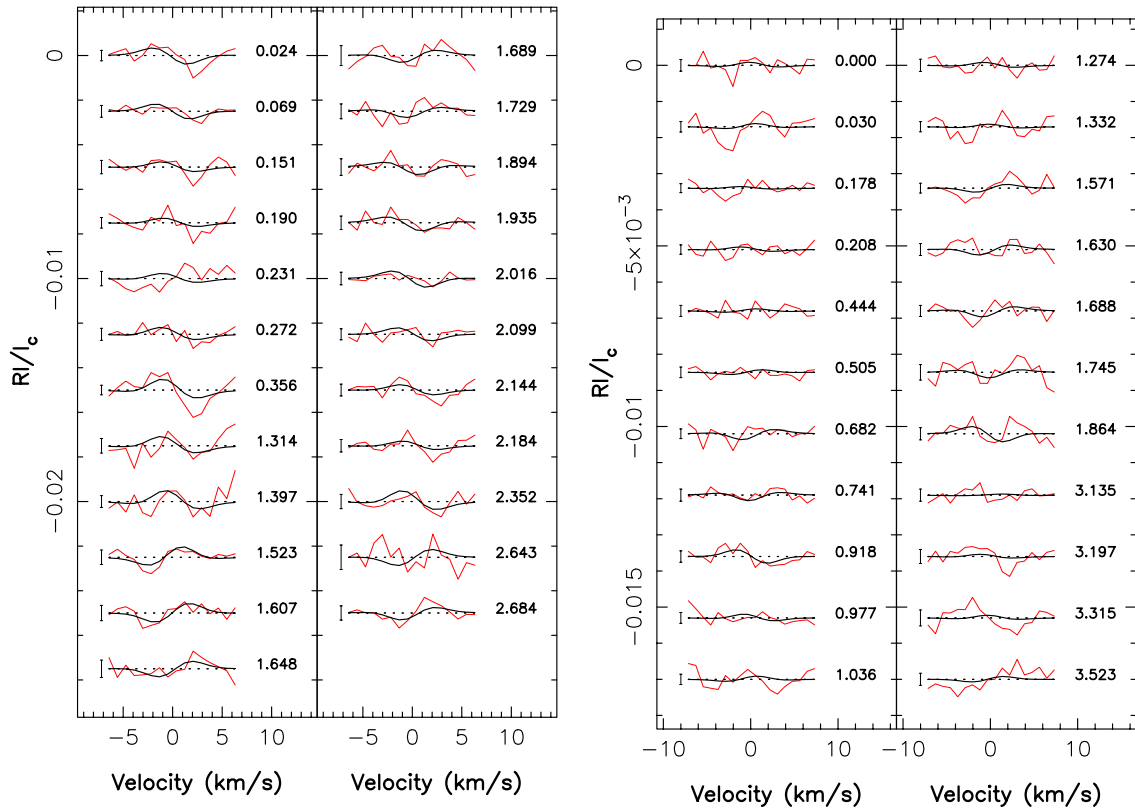
Figure E1. As Figure 6 for GJ 479.



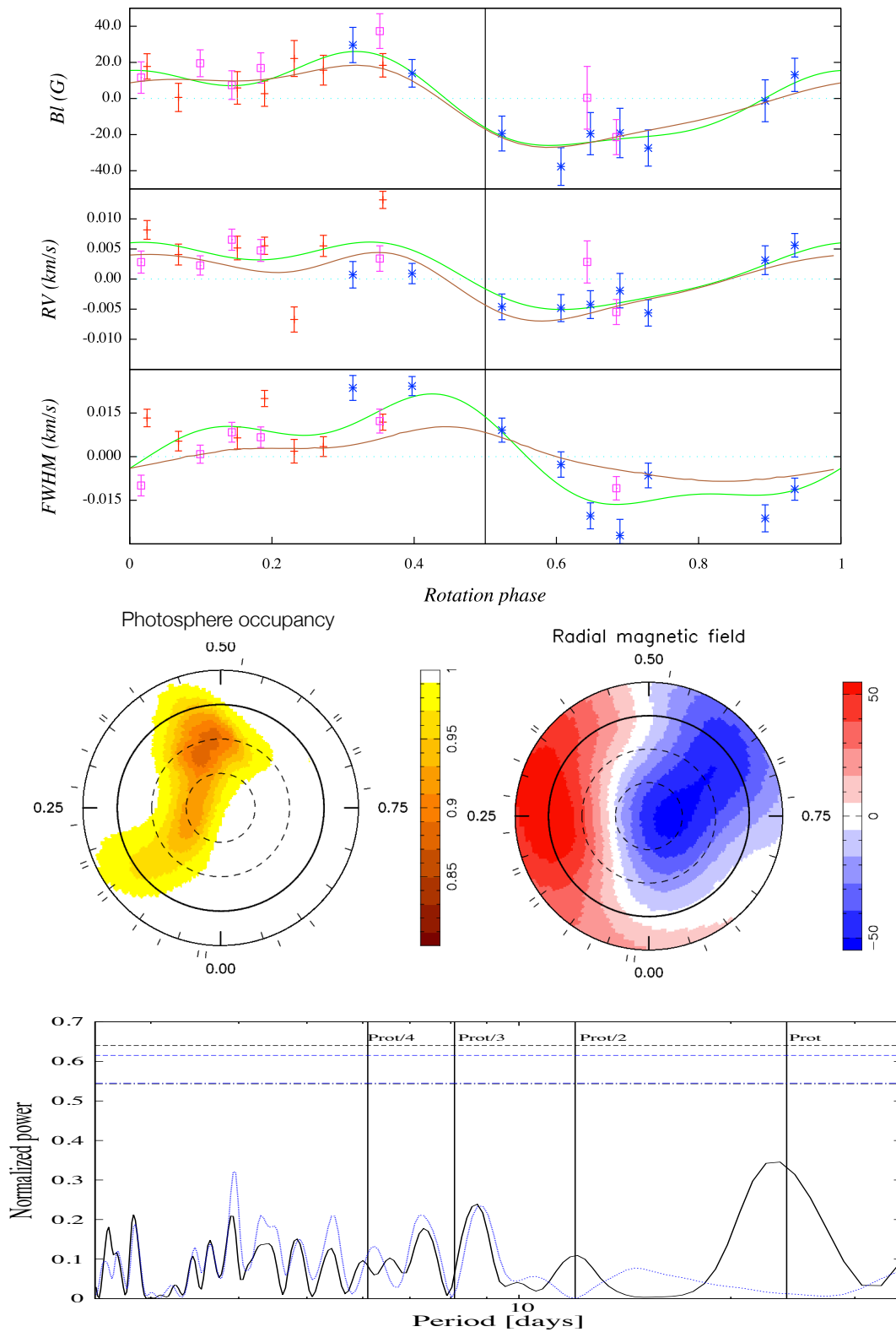
**Figure E2.** As Figure 7 for GJ 205. Note that for this star, the DR is supposed only, and not measured from the data set.



**Figure F1.** Reconstructed map obtained for a star with  $v \sin i = 1 \text{ km s}^{-1}$  and  $i = 60^\circ$  with 2 spots covering 1.5% of the stellar surface. *Left:* Reconstructed map from  $I$  with the sampling  $A$ , *Right:* Reconstructed map from  $RI$  with the sampling  $A$ . The colour-scale depicts the photosphere filling factor of each cell (white corresponding to a spotted cell).



**Figure G1.** Same as Figure 9 for GJ 479 (left) and GJ 205 (right).

**Figure H1.** Same as Figure 10 for GJ 479



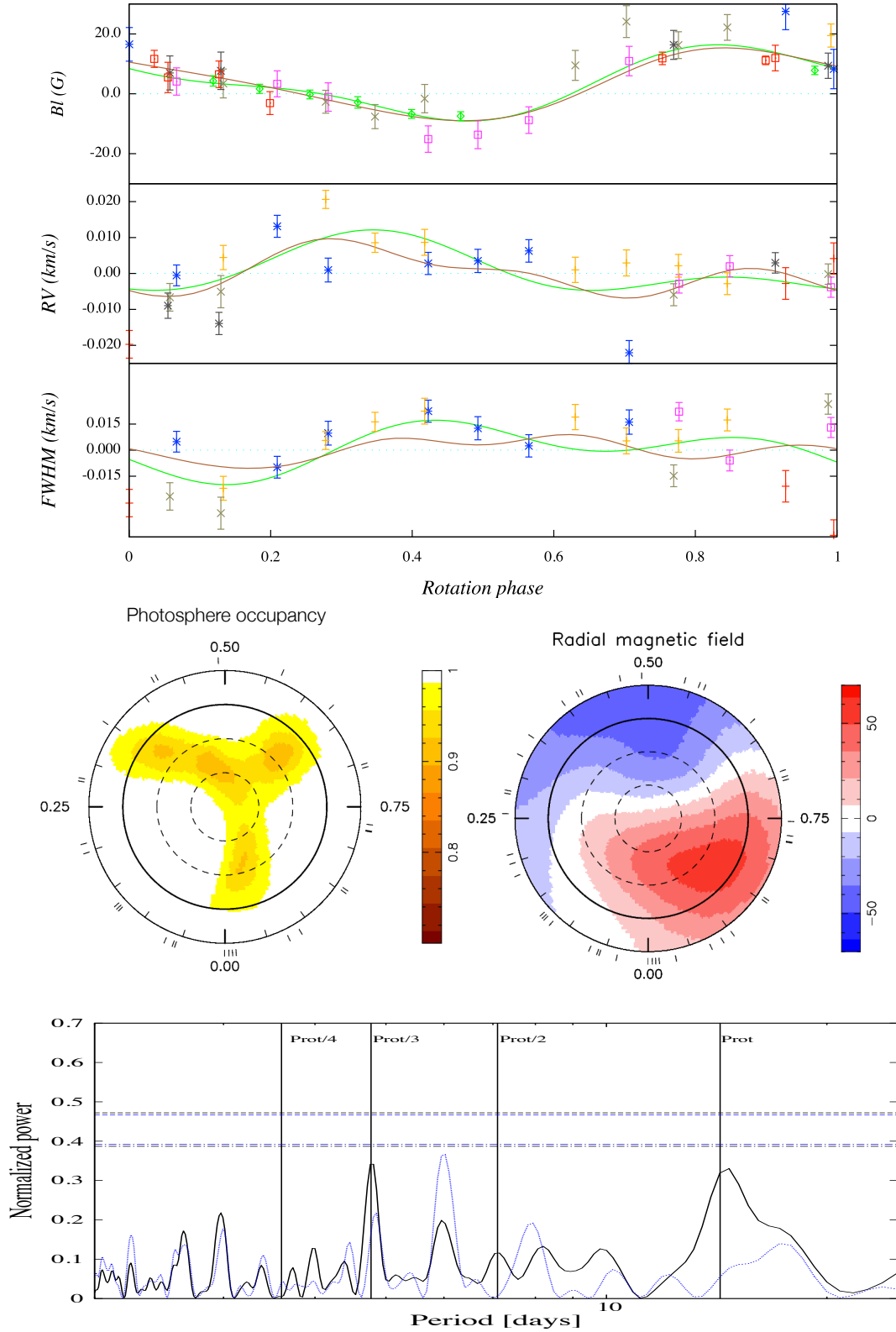
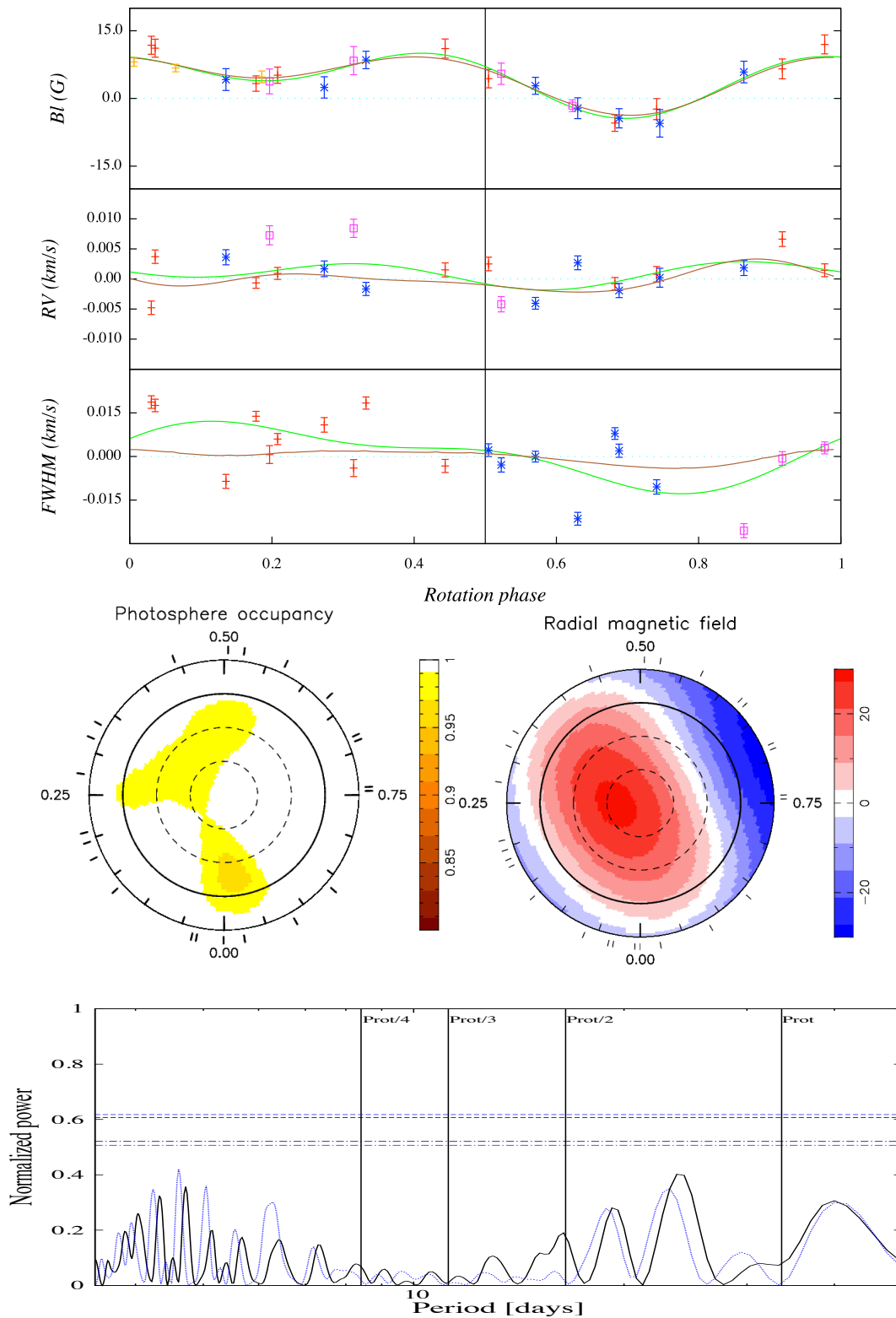


Figure H2. Same as Figure 10 for GJ 410, from the whole data set.



**Figure H3.** Same as Figure 10 for GJ 205